Tectonics®

RESEARCH ARTICLE
10.1029/2024TC008535

Key Points:

- A latest Jurassic to Early Cretaceous syn-collisional trench sequence has been discovered in central Tibet
- The trench basin recorded detritus from multiple sources, including the Dongkaco microcontinent and accreted components
- Microcontinent collision and accretion formed a strong, rigid basement for the Cenozoic Lunpola basin in central Tibet and influenced subsequent uplift

Supporting Information:

Supporting Information may be found in the online version of this article.

Correspondence to:

X. Hu,
huxm@nju.edu.cn

Citation:

Ma, A., Hu, X., Chew, D., Liang, W., Wen, D., & Deng, T. (2025). A latest Jurassic to Early Cretaceous syn-collisional trench sequence in central Tibet recorded the role of microcontinents in Lhasa–Qiangtang collision. *Tectonics*, *44*, e2024TC008535. https://doi.org/10.1029/2024TC008535

Received 27 JUL 2024
Accepted 22 FEB 2025

Author Contributions:

Conceptualization: Anlin Ma, Xiumian Hu
Funding acquisition: Xiumian Hu
Investigation: Anlin Ma, Dingjun Wen, Tao Deng
Methodology: Anlin Ma, David Chew, Wendong Liang
Supervision: Xiumian Hu
Visualization: Anlin Ma
Writing – original draft: Anlin Ma
Writing – review & editing: Xiumian Hu, David Chew, Wendong Liang, Dingjun Wen, Tao Deng

A Latest Jurassic to Early Cretaceous Syn-Collisional Trench Sequence in Central Tibet Recorded the Role of Microcontinents in Lhasa–Qiangtang Collision

Anlin Ma[1], Xiumian Hu[1], David Chew[2], Wendong Liang[3], Dingjun Wen[4], and Tao Deng[1]

[1]State Key Laboratory of Mineral Deposits Research, School of Earth Sciences and Engineering, Nanjing University, Nanjing, China, [2]Department of Geology, School of Natural Sciences, Trinity College Dublin, Dublin, Ireland, [3]State Key Laboratory of Oil and Gas Reservoir Geology and Exploitation, Institute of Sedimentary Geology, Chengdu University of Technology, Chengdu, China, [4]State Key Laboratory of Nuclear Resources and Environment, East China University of Technology, Nanchang, China

Abstract As the most recent collisional event prior to the early Cenozoic India-Asia collision, the suturing of the Lhasa-Qiangtang terranes resulted in crustal accretion and the formation of lithospheric structures that greatly influenced subsequent Cenozoic rock uplift in central Tibet. The discovery of several microcontinents within the Bangong-Nujiang suture zone between the Lhasa and Qiangtang terranes potentially implies multiple suturing stages, however, how and when the suturing of these terranes occurred are highly disputed. Here, we present a newly discovered latest Jurassic to Early Cretaceous deep-marine gravity-fan succession that is over 660 m thick in the Jienu Mountain region, south to the Cenozoic Lunpola basin. By employing multi-proxy, single-grain provenance analysis and forward modeling of sediment mixtures, we find the detritus was deposited in a syn-collisional trench and was sourced from the Dongkaco microcontinent, the obducted ophiolite—subduction complex, the accreted seamounts, and the volcanic arc rocks. We interpret that this trench deposition occurred due to the latest Jurassic to Early Cretaceous collision of the Lhasa terrane beneath the Dongkaco microcontinent and other accreted components. The sutured Dongkaco microcontinent forms the basement to the Lunpola basin and is inferred not present beneath the narrower Nima, Gaize, and Awenco basins along strike to the west where these basins are either narrower or exhibit abrupt facies changes with time. This study highlights the importance of Mesozoic tectonic inheritance on subsequent Cenozoic uplift of the Tibetan Plateau.

Plain Language Summary The Tibetan Plateau was uplifted due to multiple continental collisions over the past 250 million years. The earlier collisions established a foundation for, and even controlled, the surface uplift during subsequent collisions. The inherited structure and topography may be crucial for the spatially varied uplift of Tibet over the last 60 million years since the India-Asia collision but has not been demonstrated by case studies. In this study, we provide evidence from a deep marine trench sequence in central Tibet. The strata consist of conglomerate and sandstone sourced from various rocks, including a microcontinent, volcanic arc, accretionary prism, and ancient seamount. These strata were deposited in a period between 147 and 122 million years ago. The deposition likely indicates a syn-depositional collision between the Lhasa to the south and a microcontinent attached to the Qiangtang terrane to the north, just after the microcontinent-Qiangtang collision. The suturing process involving the microcontinent between Lhasa and Qiangtang established a stable and rigid base, above which the largest continental basin (compared to others along strike without a microcontinent base) developed later and remained low in elevation for a long time.

1. Introduction

The rise of the Tibet-Himalaya orogen significantly influenced global Cenozoic cooling, the development of the Asian monsoon, as well as the biodiversity and water resources across Asia (Molnar et al., 1993; Spicer et al., 2025). It has been well documented that incorporation of several ribbon continents during the Mesozoic to Cenozoic contributed to the amalgamation and corresponding rise of Tibet-Himalaya (Dewey et al., 1988; Ding et al., 2022; Kapp & DeCelles, 2019; Murphy et al., 1997). The suturing of Lhasa andQiangtang terranes, as the most recent collisional event before early Cenozoic India-Asia collision, lead to the formation of the Bangong-Nujiang suture zone upon which are sited a series of Cenozoic basins, such as the Lunpola, Nima, Gaize, and Awenco basins from east to west (Figure 1a). Among these basins, the Lunpola basin has the largest extent

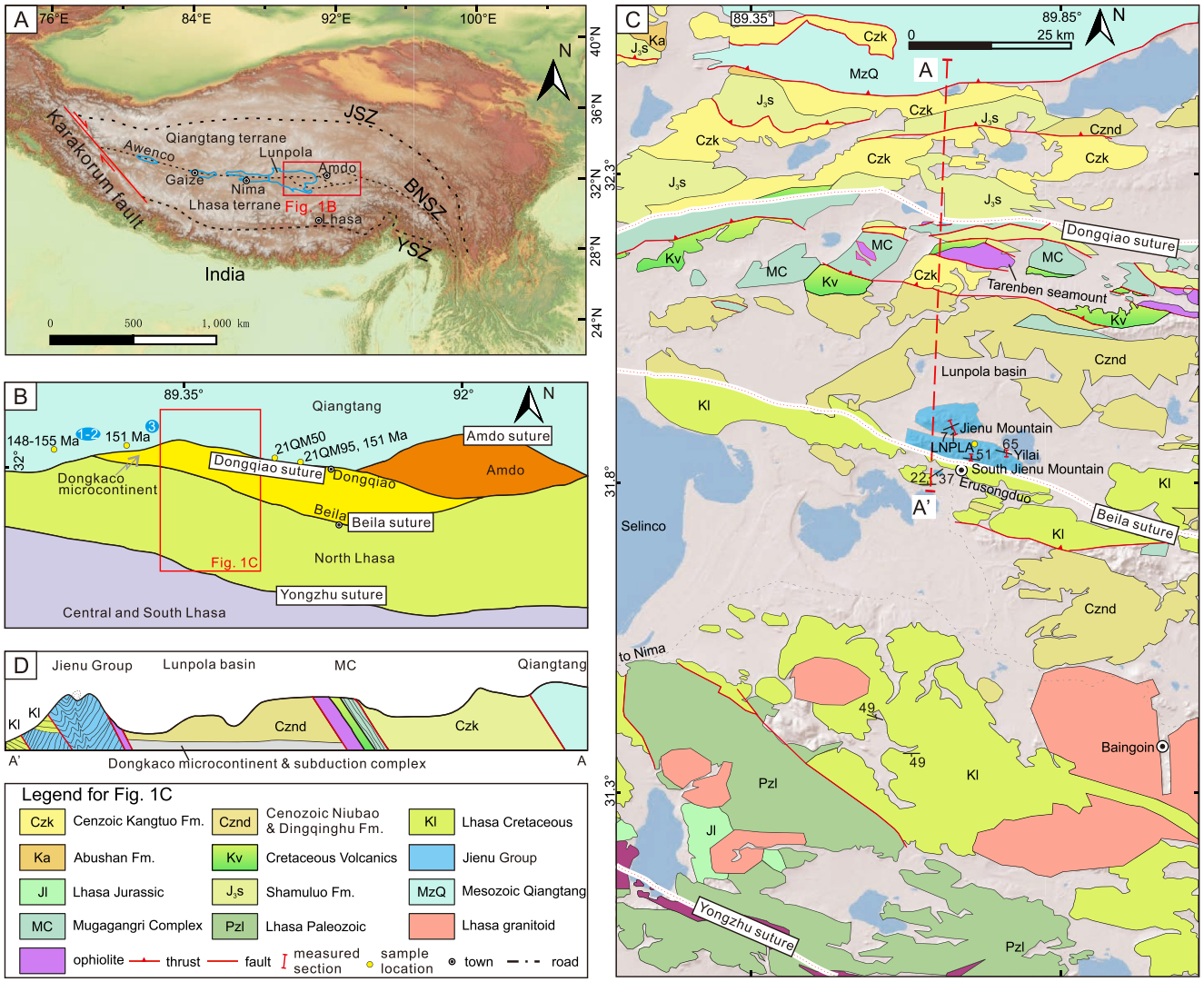

Figure 1. Geological map of the study area. (a) Regional digital evolution model of the study area in central Tibet, showing the Cenozoic basins (delimited by blue lines) along the Bangong-Nujiang Suture Zone (BNSZ) and the location of panel b (red box) (L. Wang et al., 2011). JSZ: Jinsha suture zone, YSZ: Yarlung suture zone. (b) The Dongkaco and Amdo microcontinents within the Bangong-Nujiang suture zone. Late Jurassic magmatic rocks with ages indicated and references noted in blue background: 1, Y. Li et al. (2016); 2, Yang et al. (2021); 3, A. Ma et al. (2018). (c) Geological map of Jienu Mountain and adjacent areas (modified from 1:250000 China Geological Survey maps, https://geocloud.cgs.gov.cn/). (d) Cross section (A-A′) showing the structural relationship between different units.

(Figures 1a–1c). Some studies suggest the Lunpola basin attained high elevations in the Eocene and was part of a proto-Tibetan Plateau based on oxygen isotopes of paleosols (Rowley & Currie, 2006) and thermochronology (Rohrmann et al., 2012; C. Wang et al., 2008). However, recent evidence from fossils of fishes (Wu et al., 2017) and plants and leaves (Su et al., 2019, 2020), carbonate clumped isotopes (L. Li et al., 2024; Xiong et al., 2022), foraminifera (Wei et al., 2016), and isotope-enabled general circulation models (Farnsworth et al., 2023) suggests it represented a humid, low-elevation valley along the Bangong suture zone during the Eocene (see the review of L. Li et al. (2022)).

Tectonic inheritance from the Mesozoic terrane-bounding sutures has been implicated in the development of the basins along the Bangong-Nujiang suture, but it remains a puzzle why these basins maintained low elevations between high mountains following the initial India-Asia collision (Ding et al., 2022; L. Li et al., 2022). The westward younging Lhasa-Qiangtang collision (Ma, Hu, Garzanti, et al., 2024) may explain why the west central Tibet was lower in elevation compared to the east during the early Cenozoic (L. Li et al., 2022), but no models have been proposed for the along-strike variations in basin extents. Reconstructing the suturing history between

the Lhasa-Qiangtang terranes can reveal how the Bangong-Nujiang suture zone evolved from a deep trench to a low-elevation valley and finally became part of the high-elevation plateau. Microcontinents, not uncommon in the Bangong-Nujiang Ocean (Chen et al., 2002; Guynn et al., 2006), may have played important roles in the Lhasa-Qiangtang suturing and influenced subsequent paleogeographic evolution along the Bangong-Nujiang suture zone. However, the suturing processes involving the Lhasa, Qiangtang, and microcontinents are still debated due to a lack of robust evidence (X.-M. Hu et al., 2022; Kapp & DeCelles, 2019; S. Li et al., 2019).

In the Dongqiao-Beila region, the Dongkaco microcontinent is comprised of well-exposed Paleozoic quartzite and limestone strata within the Bangong-Nujiang suture zone (between the Dongqiao suture in the north and the Beila suture in the south) (Chen et al., 2002; Girardeau et al., 1984; X.-M. Hu et al., 2022; Ma, Hu, Li, et al., 2024; Figure 1c). The collision between the Qiangtang terrane and the Dongkaco microcontinent is well constrained to late Middle Jurassic to Late Jurassic by characterization of syn-orogenic deposits in south Qiangtang and the northern branch of the Bangong-Nujiang suture zone (A. Ma et al., 2017, 2018, 2023; Ma, Hu, Kapp, BouDagher-Fadel, & Lai, 2020). The Dongkaco microcontinent and its associated sutures may extend tens of kilometers along strike westward beneath the thick Cenozoic strata of the Lunpola basin (Figure 1b), although this remains uncertain due to a lack of outcrop.

In this study, we focus on the dispersed Jurassic to Cretaceous deep-marine rocks surrounding the Lunpola basin, as they may record the marine regression and terrane accretion history. We apply detailed stratigraphy, sedimentology, and multiple single-grain provenance proxies to reconstruct the depositional history of these newly discovered submarine fan deposits to determine the tectonic setting of the basin, to reconstruct the Lhasa-Qiangtang suturing history, and to constrain the role of tectonic inheritance on the development of the Cenozoic basins within central Tibet.

2. Geological Background

The Bangong-Nujiang suture zone, extending roughly in an east-west direction for over 2,000 km, divides the Qiangtang terrane to the north from the Lhasa terrane to the south. It represents the location where the Bangong-Nujiang Tethyan ocean was subducted and finally closed, with oceanic remnants including ophiolite, siliciclastic mélange, and sparse metamorphic rocks which are mainly Jurassic in age (X.-M. Hu et al., 2022). The Bangong-Nujiang Ocean experienced a contrasting evolution along strike (X.-M. Hu et al., 2022; Ma, Hu, Garzanti, et al., 2024). In the Selinco to Amdo regions, the Bangong-Nujiang suture zone is subdivided into the Dongqiao suture in the north and Beila sutures in the south (Figure 1b), separating from north to south the Amdo microcontinent, the Dongkaco microcontinent, and the North Lhasa terrane, respectively (Figure 1b). The Dongkaco microcontinent is comprised primarily of Paleozoic quartz sandstone with detrital zircons showing an affinity with the Lhasa terrane (Chen et al., 2002; Girardeau et al., 1984; Ma, Hu, Li, et al., 2024), while the Amdo microcontinent is comprised of paragneiss and quartzite with an affinity to the Qiangtang terrane (Guynn et al., 2012). The Dongqiao Ocean, a branch of the Bangong-Nujiang Ocean, was partially filled during the Late Jurassic, with the syn-orogenic subaerial to shallow marine Shamuluo and Dongqiao formations deposited over the subduction complex and obducted ophiolite, respectively (A. Ma et al., 2018; A. Ma, Hu, Kapp, BouDagher-Fadel, & Lai, 2020). Aptian continental red beds were then deposited unconformably over all the marine deposits within the Bangong-Nujiang suture (Z. Zhu et al., 2019).

The Qiangtang terrane is comprised mainly of Jurassic shallow marine to shelf sedimentary rocks, along with the latest Middle Jurassic synorogenic conglomerate and sandstone of the Biluoco Formation in the southern Qiangtang basin (A. Ma et al., 2017). Marine deposition terminated in the Late Jurassic to the earliest Cretaceous (A. Ma et al., 2023). The Lhasa terrane is transected by the Shiquanhe-Asuo-Yongzhu suture, which divides northern Lhasa from central Lhasa. Late Jurassic ophiolites are found along the Yongzhu suture and this suggests the Yongzhu Ocean may have persisted into the Latest Jurassic (S. Fan et al., 2017; Tang et al., 2020).

The Jienu Group within the Bangong-Nujiang suture zone was first established in the Jienu Mountain region by the Xizang Geological Survey team in 1983 (Xia & Liu, 1997; Figure 1c). This unit, with a thickness of nearly 1.2 km, is dominated by conglomerate and sandstone with minor mudrock, volcanic rock and limestone, and has an inferred Middle to Late Jurassic depositional age based on bivalves (*Praeexogyra acuminata*, *Lopha gregarea*, *Meleagrinella* cf. *ovalis*, *Lima* sp., ? *Gresslya abducta*, *Astarte* sp., *Coelopis* sp., ? *Fimbria dingriensis*), gastropods (*Nerinea* sp.), and ammonites (*Protetragonites* sp., *Himalayites* sp., *Lilloetia* sp., *Pseudocadoceras* cf. *pelelini*) (Xia & Liu, 1997). Since then, this unit has been regarded as either a unit of the north Lhasa terrane

underlying the Late Jurassic to Early Cretaceous Lagongtang Formation (D.-C. Zhu et al., 2016), as a forearc basin (S.-M. Li et al., 2020) or as a trench/trench slope basin (Z. Zhu et al., 2022) within the Bangong-Nujiang suture zone as a result of northward oceanic subduction during the Jurassic (Figure S1 in Supporting Information S1). Provenance studies have suggested the Jienu Group was sourced from the Qiangtang terrane (S.-M. Li et al., 2020).

3. Methods

We first conducted field investigation on the Jienu Group to determine conglomerate clast compositions, interpret the sedimentary environments, and collect samples for depositional age constraints and provenance analysis (sample information in Table S1 in Supporting Information S2). We characterized the sandstone petrology and detrital heavy mineral suites, and employed multiple-proxy geochemical and geochronological methods on the latter. The U-Pb ages of detrital zircons from the sandstones were determined to constrain the maximum depositional age and interpret the provenance. The age and provenance interpretations were supplemented by U-Pb geochronology of zircons and/or apatites from both volcanic clasts within the conglomerate and volcanic rocks in the potential source area(s). We also undertook the zircon trace element analysis and determined whole-rock major and trace element abundances of volcanic rocks from both the source and the sink to further reveal their tectonic settings. Since the sandstone contains significant basaltic rock fragments, which cannot be traced with zircons (which are rare in mafic rocks), we used the major elements of detrital Cr-spinels to constrain this portion of the provenance contribution (e.g., Cookenboo et al., 1997; X.-M. Hu et al., 2014; Ma, Hu, Kapp, BouDagher-Fadel, & Lai, 2020).

3.1. Field Geology and Samples

Detailed logging and sedimentological observations were undertaken on three measured sections (Jienu Mountain, south Jienu Mountain, and Yilai) and one outcrop (West Erusongduo) to determine the stratigraphy and sedimentary environments. Stratigraphic sections were measured with a tape on 1:200 section logs. The lithofacies analysis is based on sedimentary structures and textures and primarily follows Miall (1977) and Pickering and Hiscott (2015). As most of the lithofacies in the Jienu Group have been documented in the literature, we provide only brief descriptions and include a summary table listing standard interpretations of physical processes (Table 1). Conglomerate clast counts were determined by counting ca. 100 clasts at each of the 11 sites, using a grid tailored to the clast size at each site. The clast lithology proportion data are reported in Table S2 in Supporting Information S2.

3.2. Sandstone Petrography and Heavy Minerals

Twenty-one sandstones, with no weathering surfaces and late veins, were selected for optical petrographic analysis, including 11 from the Jienu Mountain section, three from the Yilai section, three from the south Jienu Mountain section, and two from the West Erusongduo section. Detrital modal abundances of the sandstones were determined by ca. 400 point counts per thin section under a polarizing microscope following the Gazzi-Dickinson method, in which crystals/grains larger than 62.5 μm in diameter within rock fragments are counted as single grains (Ingersoll et al., 1984). The modal abundances were normalized for plotting on standard QFL (Q = quartz; F = feldspar; L = lithics; sandstone classification after Garzanti (2019)) and LvLmLs (Lv = volcanic; Lm = metamorphic; Ls = sedimentary) ternary diagrams. The results are presented in Table S3 in Supporting Information S2.

Heavy minerals were separated from two samples by centrifuging in Na-polytungstate (2.90 g/cm^3), made into a slide with Canada balsam, and then point counted under a polarized microscope. More than 200 transparent heavy minerals were counted using regular spacing on each mount. The complete data sets are provided in Table S4 in Supporting Information S2.

3.3. U-Pb LA-ICP-MS Dating of Zircon and Apatite

Rock samples were crushed and heavy minerals were separated by heavy liquid and magnetic separation. Zircon grains were mounted in epoxy and polished to expose grain interiors. Cathodoluminescence (CL) images of zircons were acquired using an analytical scanning electron microscope (TESCAN MIRA3), with an accelerating voltage of 7 kV to reveal their structure and zonation patterns. In total, 506 zircons were dated by LA-ICP-MS.

Table 1
Lithofacies for Sedimentary Rocks With Interpretations of Their Depositional Processes, Modified After Miall (1977) and Pickering and Hiscott (2015)

Lithofacies code	Description	Interpretation
Gmm	Massive, matrix-supported, pebble to boulder, poorly sorted with enormous blocks or olistoliths, disorganized, unstratified	Deposition by cohesive mud-matrix debris flows and blocky flows. Enormous blocks may slide into place on a cushion of overpressured or liquefied mud
Gcm	Massive, clast-supported, pebble-cobble, poorly sorted, disorganized, unstratified	Deposition from concentrated clast-rich debris flow, density flows, and inflated gravel flows
Gch	Clast-supported, pebble to cobble, medium-well sorted, horizontally stratified	Grain-by-grain deposition from suspension and then traction transport as bed-load, indicating to concentrated density flows
Ghi	Clast-supported, pebble to cobble, well-sorted, horizontally stratified, imbricated (long-axis transverse to paleoflow)	Grain-by-grain deposition from suspension and then traction transport as bed-load, indicating to concentrated density flows
Sm	Massive medium to coarse-grained sandstone, sometimes pebbly and lens-like	High rate of deposition, high-concentrated density flows, probably formed during high-discharge periods
Sh	Medium to very coarse-grained sandstone, horizontally stratified, sometimes pebbly	Repeated burst-sweep cycles with varying flow energy in concentrated density flows
Sr	Fine to medium grained sandstone, with asymmetric 2D and 3D current ripples	Migration of small 2D and 3D ripples under weak unidirectional flows
F	muds, silty muds and clays, typically structureless, locally laminated	Suspension-setting or rapid deposition in mud-rich turbidity currents

These include 320 detrital zircon grains from five samples, 20DK90 (n = 90), 20DK95 (n = 77), 20DK108 (n = 46), 20DK100 (n = 30) and 20DK107 (n = 77) that were analyzed at the State Key Laboratory of Mineral Deposits Research, Nanjing University (MiDeR-NJU) using an Agilent 7500a quadrupole(Q) ICP-MS coupled to a GeoLas Pro 193 nm laser ablation (LA) system. A total of 32 magmatic zircon grains were dated in samples 21SL146 (n = 12) and 21QM95 (n = 20) using an ASI Resolution S-155 193 nm ArF Excimer laser coupled to a Thermo Scientific iCAP Qc Q-ICP-MS, also at MiDeR-NJU. A total of 154 zircon analyses were undertaken on samples 21QM95 (n = 20), 20DK95 (n = 29), 20DK108 (n = 45), and 20DK100 (n = 60) at Nanjing Hongchuang Exploration Technology Service Co., Ltd using a Teledyne Cetac 193 nm G2 LA system coupled to an Agilent 7900 Q-ICP-MS. Analytical methods are described in detail in A. Ma et al. (2023). U-Pb isotopic and geochronological data with 2σ uncertainty are reported in Table S5 in Supporting Information S2. The diagrams of concordia and weighted mean $^{206}Pb/^{238}U$ ages of monitor standards, including Plešovice (337 ± 3 Ma, MSWD = 0.6, n = 6), Mud Tank (730 ± 7 Ma, MSWD = 0.2, n = 21), and GEMOC GJ-1 (604 ± 1 Ma, MSWD = 0.8, n = 28), are provided in Figure S8 in Supporting Information S1. The ages of these monitor standards align with their recommended values (Black & Gulson, 1978; Jackson et al., 2004; Sláma et al., 2008).

The trace element abundances of the magmatic zircon samples 21SL146 (n = 12) and 21QM95 (n = 40) were simultaneously acquired during the LA-ICP-MS dating procedure. For trace element calibration, the standard glass NIST610 was used as the primary reference with ^{29}Si employed as the internal elemental standard (Y. Liu et al., 2010). Ti-in-zircon crystallization temperature was calculated following methods of Watson and Harrison (2005). Analyses of the reference materials and sample unknowns are provided in Table S6 in Supporting Information S2.

The preferred U-Pb zircon age employed $^{206}Pb/^{238}U$ ages for zircon grains <1000 Ma and $^{207}Pb/^{206}Pb$ ages for grains >1000 Ma. Grains with <30% discordance or reverse discordance ($^{206}Pb/^{238}U$ vs. $^{206}Pb/^{207}Pb$) were retained for grains >400 Ma; this cutoff was applied in order to include more grains for provenance interpretation. For grains <400 Ma, grains with only <10% discordance ($^{207}Pb/^{235}U$ vs. $^{206}Pb/^{238}U$) were retained for precise maximum depositional age estimates. The toolset *detritalPy* was used to generate histograms of U-Pb ages, kernel density estimates, and probability density plots (PDP), and calculate maximum depositional ages (Sharman et al., 2018). Detrital age signatures were compared quantitatively using multi-dimensional scaling (MDS) and forward-mixture modeling. The MDS approach compares the inferred similarities (and differences) between

samples by Euclidian distance. This study employs 3D MDS using the likeness as a basis for comparison, which was carried out through the DZmds software (Saylor et al., 2018). The forward-mixture modeling was conducted to estimate the relative contribution of potential sources to the basin. A random sampling approach ("bootstrapping") was first applied for the parent and child age distributions to characterize the uncertainty in these model predictions that results from the limited sampling of complex detrital distributions (Malkowski et al., 2019). The difference between the two distributions was determined using the Kuiper V statistic (V_{max}), which sums the maximum positive and negative differences between two cumulative distributions (Kuiper, 1960; Saylor & Sundell, 2016).

In situ U-Th-Pb isotopes of apatites from volcanic clasts in the Jienu Formation (samples 21SL146, $n = 33$; 20DK88, $n = 50$) were analyzed by an Agilent 7900 Q-ICP-MS coupled to a Photon Machines Analyte Excite 193 nm ArF excimer laser-ablation system at the Department of Geology, Trinity College Dublin, Ireland. The ablation was carried out using a 35-μm-diameter spot, with 300 shot counts at an 11 Hz repetition rate and with a 2.5 J cm^{-2} fluence. Each grain was analyzed for 25 s with a 10 s washout which was employed for the baseline measurement. The generated aerosol was transported into the mass spectrometer by pure helium gas, then mixed with argon and nitrogen gas were added to enhance signal sensitivity and reduce oxide formation. The primary and secondary reference materials were Madagascar apatite, McClure Mountain apatite and Durango apatite, respectively (Chew et al., 2014). All data reduction was performed off-line using the Iolite data reduction package (Paton et al., 2011) using the "VizualAge_UcomPbine" data reduction scheme (Chew et al., 2014). The Tera-Wasserburg plots were drawn using Isoplot 4.15 (Ludwig, 2011). Single-grain detrital apatite ages were ^{207}Pb-corrected using an iterative approach (Chew et al., 2011) using the terrestrial Pb evolution model of Stacey and Kramers (1975). The cut-off criteria for the propagated 2σ uncertainties on the ^{207}Pb-corrected ages are 25%, and for f_{206} it is 0.8. All U-Pb isotope data of apatite are reported in Table S7 in Supporting Information S2.

3.4. Cr-Spinel Major Elements

The *in-situ* analysis of Na_2O, MgO, K_2O, CaO, FeO, Cr_2O_3, SiO_2, Al_2O_3, NiO, MnO, and TiO_2 in Cr-spinel grains was carried out at the School of Geoscience and Technology, Southwest Petroleum University (Chengdu, China), using a JEOL JXA-8230 electron probe microanalyzer. The detrital Cr-spinel grains were analyzed from one sandstone clast sample 20DK107 ($n = 35$) and two sandstone samples 20DK90 ($n = 50$) and 20DK95 ($n = 33$) in the Jienu Group. Measurements were made at 15 kV accelerating voltage with a 20 nA beam current, and a 1 μm spot size. Before analysis, samples were uniformly carbon-coated (20 nm thick). The international SPI standards used were $NaAlSi_3O_8$ (Al and Si), $MgCaSi_2O_6$ (Mg and Ca), TiO_2 (Ti), $FeCr_2O_4$ (Fe and Cr), and $CaMnSi_2O_6$ (Mn). The detection limit was ±0.01 wt%. Data are reported in Table S8 in Supporting Information S2.

3.5. Major and Trace Element Analysis

Whole-rock major and trace element concentrations for volcanic rocks in the Dongqiao suture zone ($N = 2$) and clasts in the conglomerate of the Jienu Group ($N = 8$) were measured using X-ray fluorescence (XRF, Zsx Primus II) and inductively coupled plasma mass spectrometry (ICP-MS Agilent 7700e), respectively, at the Wuhan Sample Solution Analytical Technology Co., Ltd., Wuhan, China (data are reported in Tables S9 and S10 in Supporting Information S2). For major-element analysis, the sample powder (200 mesh, 74 μm) was oven-dried at 105°C for 12 hr. Loss on ignition (LOI) was determined by measuring the weight loss after heating in a muffle furnace at 1000°C for 2 hr. The sample powder was mixed with a cosolvent ($Li_2B_4O_7$: $LiBO_2$: LiF = 9:2:1) and an oxidant (NH_4NO_3) in a platinum crucible, heated until molten, and finally quenched for XRF analyses. Analytical precision was 2% for major element oxides. The GBW07101-14 standard was used for quality control.

For trace-element analysis, the sample powder (200 mesh, 74 μm) was oven-dried at 105°C for 12 hr. A total of 50 mg of powder was weighed for each sample, placed in a clean PTFE (polytetrafluoroethylene) vessel, and 1 ml HNO_3 and 1 ml HF were slowly added before the PTFE vessel was put in a stainless-steel pressure jacket and heated to 190°C for >24 hr until dissolution was complete. After cooling, the PTFE vessel was opened and placed on a hotplate at 140°C and evaporated to incipient dryness; 1 ml HNO_3 was added and again evaporated to dryness; 1 ml of HNO_3, 1 ml of Milli-Q water, and 1 ml of a 1 ppm internal standard solution was added, and the PTFE vessel was resealed and heated at 190°C for >12 hr. The final solution was transferred to a clean polyethylene bottle and diluted to 100 g with the addition of 2% HNO_3.

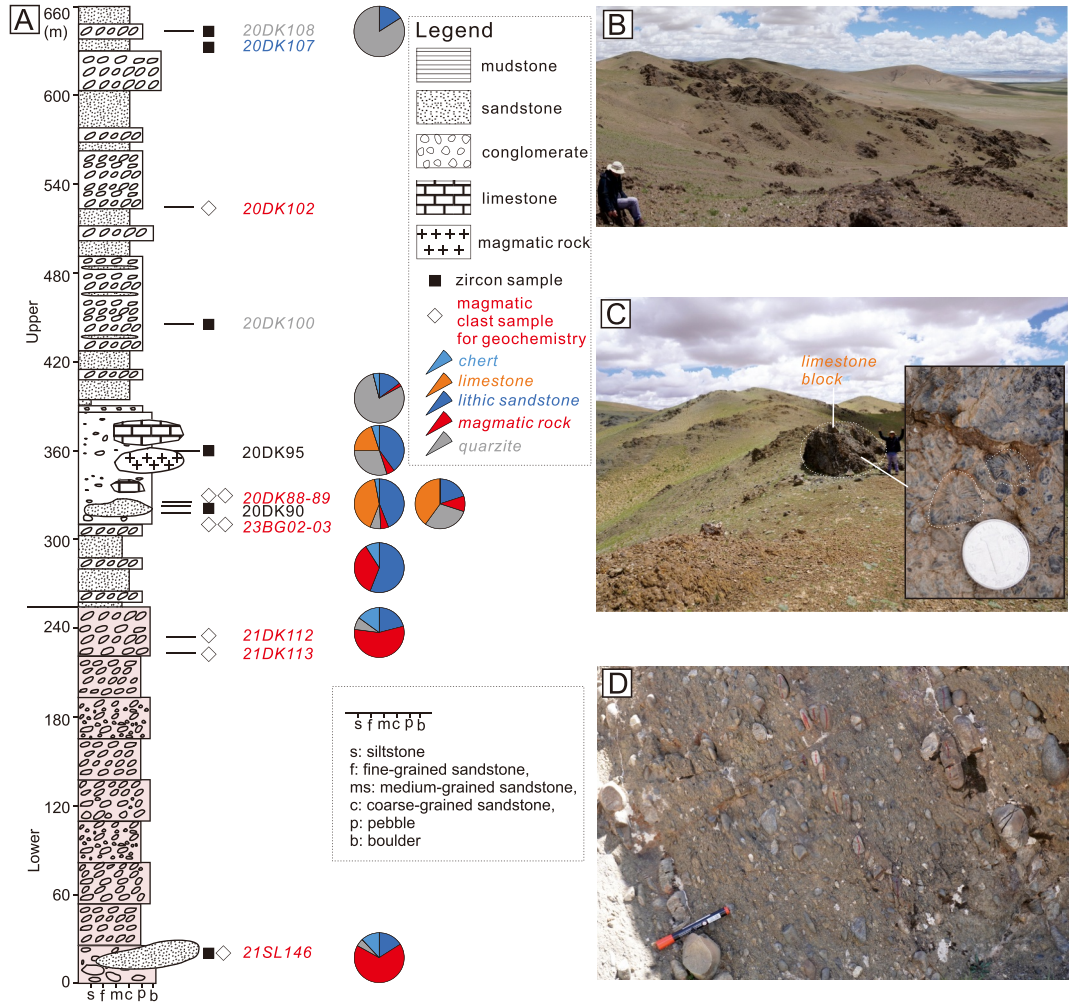

Figure 2. (a) Simplified log (left) of the Jienu Group primarily based on the Jienu Mountain section. Representative field photographs of the stratigraphy and lithofacies in this section: (b) North-dipping light-colored strata in the upper unit of the Jienu Group. (c) Massive conglomerate with outsized enormous blocks (inset shows coral fossils in a limestone block), base of the upper unit of the Jienu Group. (d) Imbricated conglomerate, middle of the upper unit of the Jienu Group.

4. Results

4.1. Stratigraphy and Sedimentology

The Jienu Group is described here from north to south (Figure 1c).

Jienu Mountain section. The Jienu Group in the Jienu Mountain section is over 660 m thick (Figure 2; Figure S2 in Supporting Information S1), although the bottom and top are poorly exposed. The Jienu Group can be divided into two subunits. The lower unit consists of ca. 250 m of dark gray, clast-supported conglomerate (Figure 2a; Figure S3a in Supporting Information S1). The conglomerate is massive (Lithofacies code Gcm) in the bottom 15 m, with outsized sandstone boulders mixed with cobbles and pebbles, and is poorly sorted with medium rounding. Up section, the conglomerates are mainly horizontally stratified (Gch, Figure 3a). The clasts are predominantly well-sorted and rounded cobbles with occasional imbrication (Ghi) in some beds. The upper unit is lighter in color, with more sandstone beds than the lower unit (Figures 2a and 2b). The first 60 m is dominated by interbedded sandstone (Sh and Sm dominated) and horizontally stratified (sometimes imbricated) conglomerate (Gch and Ghi), followed by 50 m of massive conglomerate with sandstone layers (Sh and Sm dominated). The conglomerates are matrix- (Gmm) or clast-supported (Gcm), with outsized enormous blocks (Figure 2c). The clasts are poorly sorted and exhibit medium rounding (Figure S3b in Supporting Information S1). Up section the succession becomes dominated by Gch and Ghi with some sandstone layers (Figure 2d). The clasts are mainly of

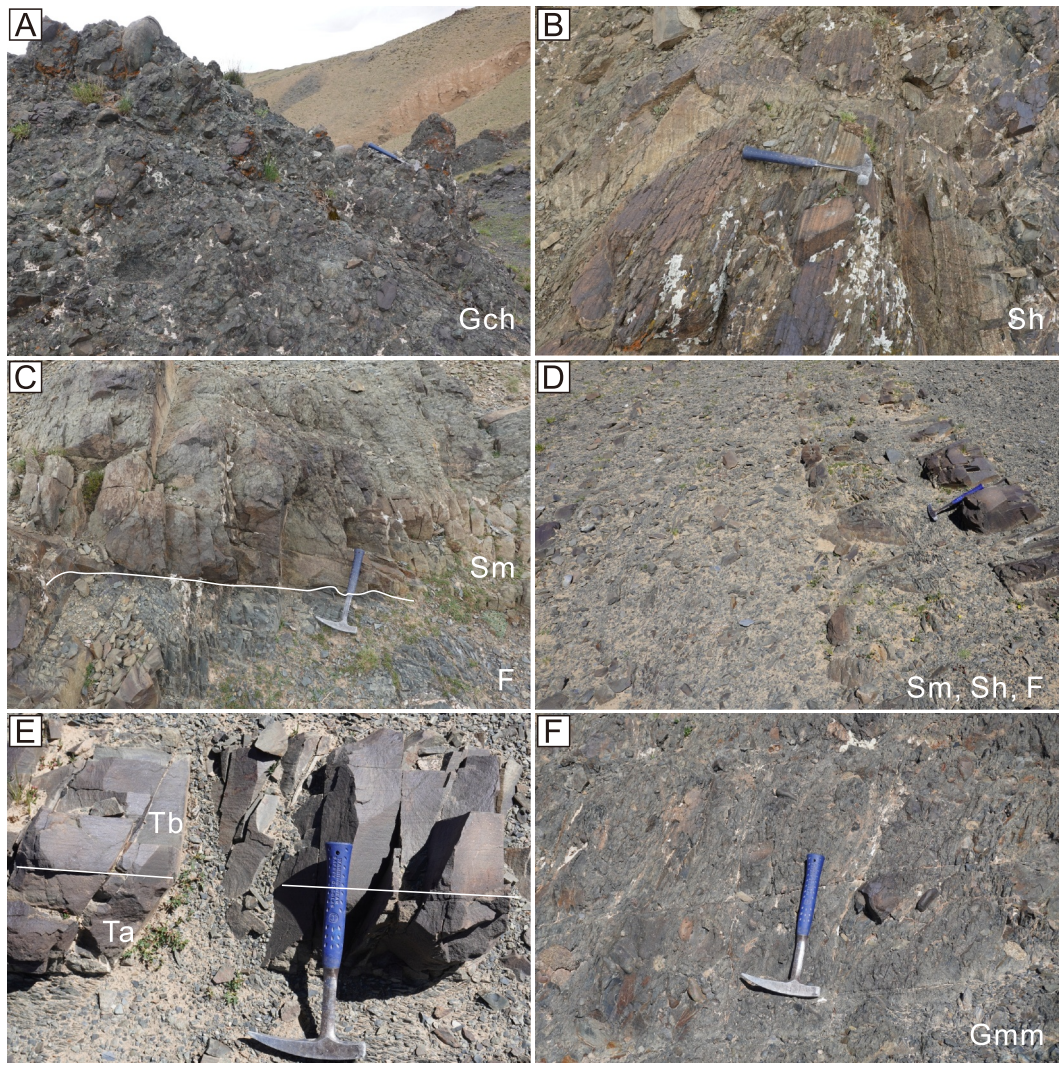

Figure 3. Field photographs showing the stratigraphy and lithofacies of the Jienu Group. (a) Horizontally stratified clast-supported conglomerate (Gch) in the lower unit of the Jienu Group, Jienu Mountain section. (b) Banded parallel-bedded sandstone (Sh), Yilai section. (c) Massive sandstone (Sm) with a scouring surface with basal siltstone, Yilai section. (d) Thinly to medium-bedded sandstone (Sm and Sh) interbedded with mudrocks, south Jienu Mountain section. (e) Bouma sequences which include massive sandstone (Ta) and sandstone with parallel laminae (Tb), south Jienu Mountain section. (f) Matrix-supported massive conglomerate (Gcm), south Jienu Mountain section.

cobble to pebble in size, and are well-sorted and rounded. The sandstones are massive (Sm), with some horizons exhibiting bedding-parallel stratification (Sh, Figures S3c and S3d in Supporting Information S1) and pebbles.

Yilai section. The Yilai section includes ca. 180 m upper unit of the Jienu Group, which mainly consists of interbedded sandstone and mudrock, with few conglomerates (Figure S2 in Supporting Information S1). The sandstones are either massive (Sm) or horizontally bedded (Sh), and are locally pebbly, with basal scour structures (Figures 3b and 3c). Mudrock intraclasts are found in the sandstones.

South Jienu Mountain section. The south Jienu Mountain section is not well exposed. We logged a ca. 80 m thick succession characterized by medium to thinly interbedded sandstone (Sm and Sh dominated) and mudrock at the base (Figure 3d) overlain by matrix-supported massive conglomerate (Gmm) (Figure S2 in Supporting Information S1; Figure 3f). The sandstone unit contains incomplete Bouma sequences which include massive sandstone (Ta) and sandstone with parallel laminae (Tb) (Figure 3e). The clasts in the conglomerate are mainly of cobble to pebble grade with a few outsized boulders, and are poorly sorted with medium rounding.

West Erusongduo. The Jienu Group in West Erusongduo crops out in small inlier surrounded by Early to mid-Cretaceous shallow marine sedimentary rocks of the northern Lhasa terrane. It mainly consists of matrix-supported massive conglomerate (Gmm) and massive pebbly sandstone (Sm), with a few outsized cobbles (Figures S3e and S3f in Supporting Information S1).

Interpretation. The sedimentological character of the Jienu Group suggests a submarine fan environment. The massive clast- or matrix-supported conglomerates (Gcm and Gmm) with outsized boulders in the Jienu Mountain section, south Jienu Mountain section, and West Erusongduo may represent olistostromes (also termed as sedimentary mélanges) (Festa et al., 2016; Pickering & Hiscott, 2015). The olistostromes could have been deposited through sliding, slumping, and debris-blocky flows in inner to middle fans, due to steep gradients and active tectonism (Festa et al., 2016). The well-organized conglomerate lithofacies, including Gch and Ghi in the Jienu Mountain and south Jienu Mountain sections, likely represent submarine channels controlled by clast-rich debris flows (Pickering & Hiscott, 2015).

In the Yilai section, the massive sandstone (Sm), with mudclast and basal scours may represent channel-fill deposits emplaced by high-density turbidity currents. These currents likely incised into underlying substrates and entrained mudclasts. The overlying horizontally bedded (Sh) and ripped (Sr) sandstones may represent levee or overbank deposits formed by waning-stage turbidity currents that spilled from adjacent channels. Interbedded mudrocks are interpreted as hemipelagic or inter-channel deposits (Pickering & Hiscott, 2015). Similarly, the recurrent alternations of sandstone (Sm and Sh dominated) and mudrock in the south Jienu Mountain section may also represent levee and inter-channel alternations, but no channelized features were found. Alternatively, these three lithofacies may constitute incomplete Bouma sequences and be interpreted as sheet-like deposits in a lobe-fringe (Mutti, 1985; Pickering & Hiscott, 2015). Overall, the southwards decrease in grain size likely implies south-directed sediment transport, though paleocurrent measurements were not systematically taken from imbricated clasts.

4.2. Multi-Proxy Sedimentary Provenance Analysis

The clasts in the conglomerate in the Jienu Group include variable amounts of basalt, chert, quartz and lithic sandstone, limestone and andesite (Figure S2 in Supporting Information S1) based on our clast counting data. The limestone contains abundant fossils including corals, bivalves, and bryozoans (Figure 2c). The color change from the darker-colored basal Jienu Group to the light-colored upper unit is reflected in the change in clast compositions. The lower unit mainly consists of basalt, chert, and minor quartzose and lithic sandstone clasts, while the clasts in the upper unit mainly consist of quartzose and lithic sandstone, basalt, and minor andesite and limestone (Figure 2a). The sandstones of the Jienu Group are lithic in composition, with an average QFL ratio of 21:13:66. The lithic fragments in the sandstones include basalt, metamorphic rocks, siliciclastic rocks, felsic volcanic rocks, chert, and limestone, with an average Lm: Lv: Ls ratio of 25:31:44 (Figure 4a; Figure S4 in Supporting Information S1). The heavy mineral assemblage in the two sandstone samples from the upper unit in the Jienu Mountain section comprises spinel, zircon, apatite, and tourmaline, with minor rutile and negligible epidote, garnet, and amphibole (Figures 4b and 4c).

To constrain the provenance of the mafic clasts, two volcanic clasts were collected and successfully analyzed for zircon and apatite U-Pb dating. Zircons from a basaltic andesite clast (21SL146) yield a concordant age at 147 ± 3 Ma (n = 3/12, MSWD = 0.2) (Figure 5a). Though only three out of twelve age datapoints are available, the CL images of these three zircons show wide unclosed bands (Figure S5 in Supporting Information S1), which is typical of zircons crystallizing from a high-temperature mafic magma (Rubatto & Gebauer, 2000). This zircon age is consistent with imprecise apatite Tera-Wasserburg lower intercept ages from the same sample of 147 ± 18 Ma (n = 33, MSWD = 1.7) and basaltic andesite sample 20DK88 (145 ± 43 Ma, n = 50, MSWD = 1.3) (Figures 5c and 5d). With the exception of sample 21SL146 which exhibits a high LOI (12.0 wt%), all other basaltic andesite samples (20DK88, 20DK89, 23BG02, and 23BG03) have moderate SiO_2 (55.3 wt%) and low TiO_2 (0.8 wt%). Trace element patterns suggest all five samples are magmatic arc-related with LREE (light rare-earth element) enrichment and depletion in HFSE (high field strength elements) (Figures 6a and 6b).

In contrast, three samples of basalt clasts (20DK102, 20DK112, and 20DK113) exhibit lower SiO_2 (45.7–49.0 wt%) and higher TiO_2 (2.5–3.3 wt%). The trace elements suggest an OIB (ocean-island basalt)-like chemistry with enrichment in HFSE, and enrichment in LREE relative to HREE (heavy rare-earth elements), with La_N/Yb_N between 5.01 and 6.71 (Figure 6). No zircon or apatite crystals were found in these three basalt samples.

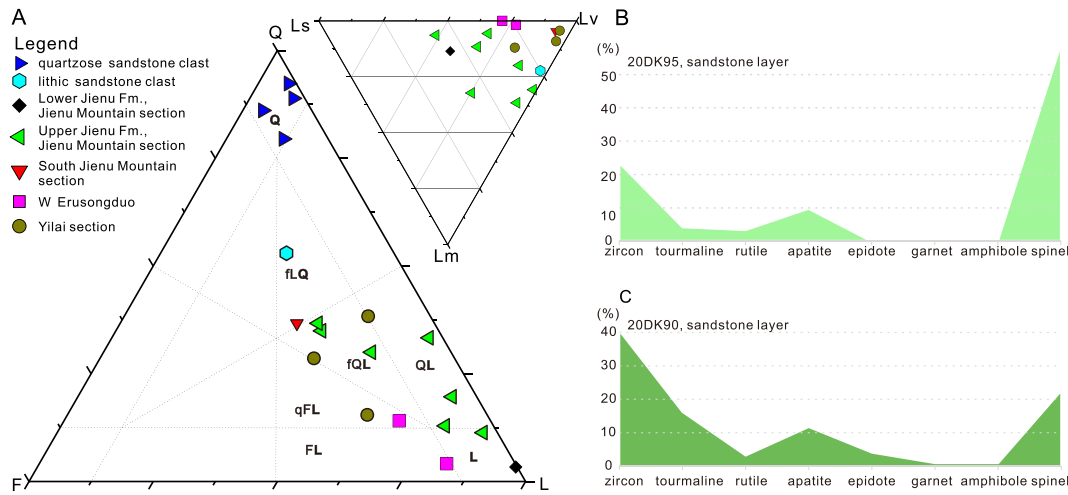

Figure 4. Framework composition of sandstone from the Jienu Group. (a) Sandstone petrography (compositional fields in QFL and LmLsLv ternary space after Garzanti (2019)). Q, quartzose; F, feldsparthic; L, lithic; FL, feldspatho-lithic; QL, quartzo-lithic; fLQ, feldspatho-litho-quartzose; fQL, feldspatho-quartzo-lithic; qFL, quartzo-feldspatho-lithic; Lv, volcanic fragment; Lm, metamorphic fragment; Ls, sedimentary fragment. (b), (c) Area chart of heavy mineral counting data from two samples from sandstone horizons in the Jienu Group.

Detrital Cr-spinels are usually sourced from mafic rocks and their major elements can be used to further distinguish the tectonic setting of their source mafic rocks (e.g., Cookenboo et al., 1997; X.-M. Hu et al., 2014; Ma, Hu, Kapp, BouDagher-Fadel, & Lai, 2020). The data from two sandstone layers (samples 20DK90 and 20DK95) and a lithic sandstone clast (sample 20DK107) in the Jienu Group suggest two sources (Figure 7), one with high TiO_2 and indicative of OIB, and the other with low TiO_2 implying a subduction-related source (Kamenetsky et al., 2001).

Sandstones from the upper unit of the Jienu Group (samples 20DK90 and 20DK95) yield similar detrital zircon U-Pb age spectra with peaks at ca. 500, 950, 1470, 1870, 2200, and 2470 Ma (Figure 8a). The 1250 Ma peak is significant in sample 20DK90 but minor in 20DK95. A lithic sandstone clast (sample 20DK107) in the Jienu Group also yields a main population at 1870 Ma, with a subpopulation population at 300–500 Ma, and minor peaks at 760 and 2430 Ma (Figure 8a). Two quartzose sandstone clasts (20DK100 and 20DK108) in the Jienu Mountain section yield similar detrital zircon U-Pb spectra, with two peaks at 550 and ca. 1000 Ma; the older peak is ca. 970 Ma in sample 20DK100 and 1100 Ma in sample 20DK108, respectively (Figure 8a).

4.3. Late Jurassic Volcanic Arc Dacites in the Source Region

Two dacite samples (21QM50 and 21QM95) collected ~35 km west of Dongqiao town within the Dongqiao suture zone are characterized by SiO_2 contents between 64.6 and 68.1 wt% and exhibit arc-like trace element features (Figures 6a and 6b) with fractionated rare earth element (REE) patterns (La/Yb = 7.0–11.8), high Sr contents (>594 ppm), low Y contents (<84 ppm), negligible Eu anomalies (Eu/Eu* = chondrite-normalized Eu/$(Sm*Gd)^{0.5}$ = 0.89–1.05), and elevated Sr/Y ratios (>70) relative to common arc rocks (Figure 6c). These geochemical features align well with those of typical adakites (Drummond et al., 1996).

Sample 21QM95 yielded zircons with a weighted mean $^{206}Pb/^{238}U$ age of 151 ± 1 Ma (n = 25/40, MSWD = 2. 9) (Figure 5b). Excluding one outlier temperature at 1295°C, the other 24 zircons yielded a mean Ti-in-zircon temperature at 737 ± 43°C (1 SD), which is slightly lower than that of basaltic andesite clast sample 21SL146 at 776 ± 53°C (n = 3, 1 SD) (Table S6 in Supporting Information S2).

5. Discussion

5.1. Depositional Ages

The stratigraphic, sedimentological, and provenance characteristics of the Jienu Group are very different from the Dongqiao-Beila region to the east. The Jienu Group in the Dongqiao-Beila region consists of black mudrock and

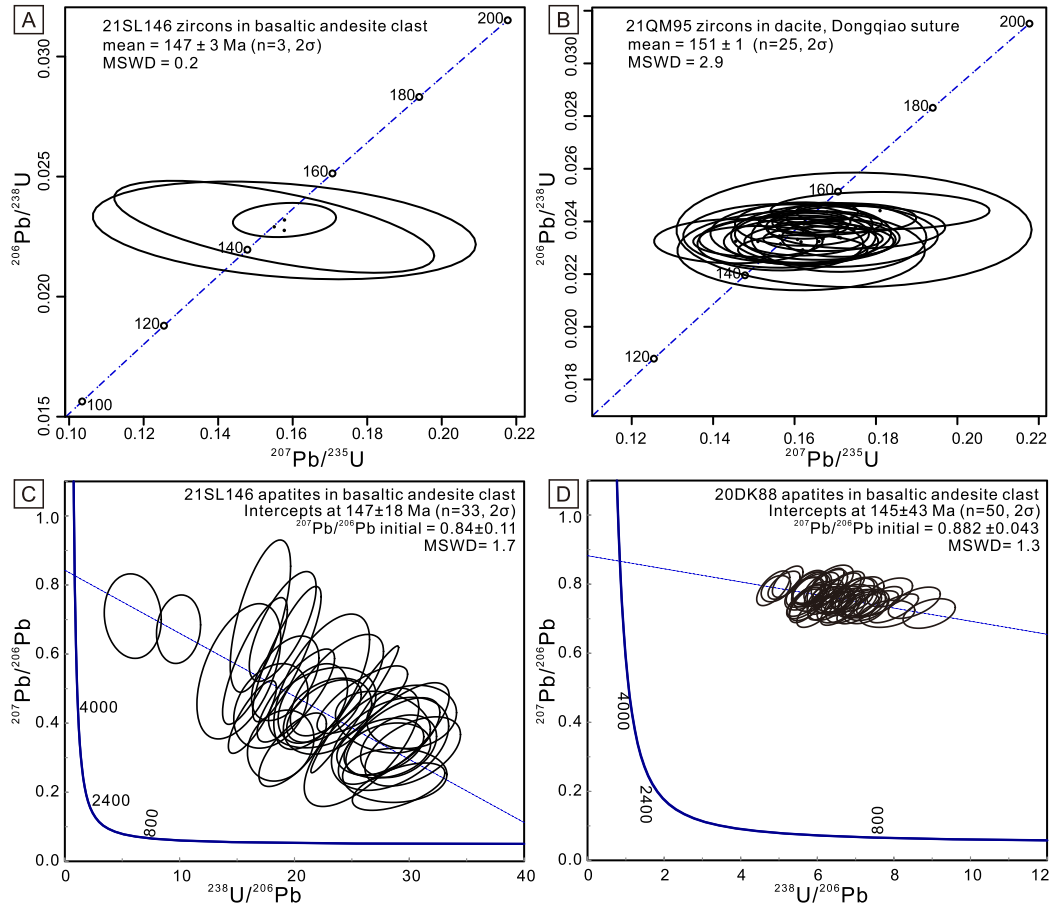

Figure 5. U-Pb dating of volcanic rocks. (a), (b) Wetherill zircon U-Pb Concordia diagrams from sample 21SL146 (basaltic andesite clast in the Jienu Group) and 21QM95 (dacite rock in the Dongqiao suture), respectively. The zircon U-Pb Concordia age from sample 21SL146 is based on 3 out of 12 analyses. (c), (d) Tera–Wasserburg U-Pb lower intercept ages for apatite from two basaltic andesite clasts (21SL146 and 20DK88) in the Jienu Group, respectively.

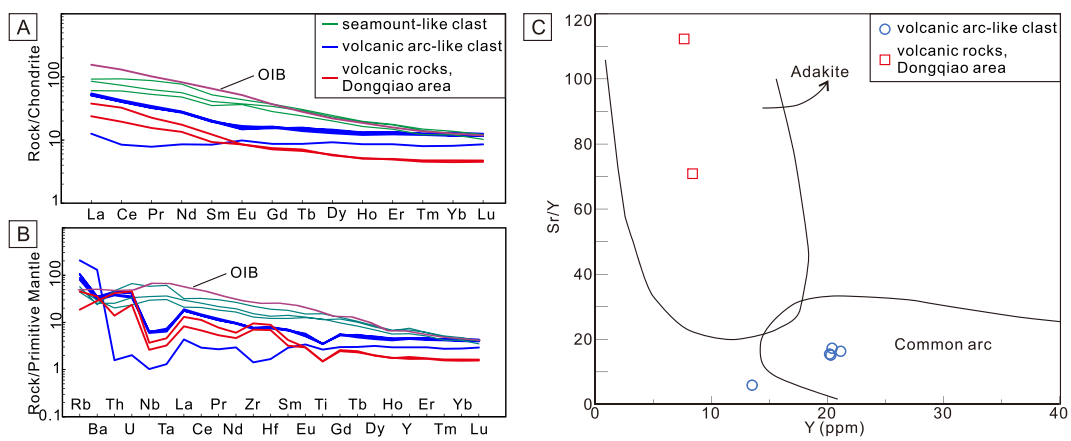

Figure 6. (a) Rare earth element diagram, (b) multi-element spider diagram, and (c) Sr/Y versus Y plot (modified after Drummond et al. (1996)) for the two types (OIB vs. arc) of volcanic clasts from the Jienu Group and volcanic rocks in the Dongqiao area. OIB (oceanic-island basalt) with data from S.-S. Sun and McDonough (1989) is plotted for comparison.

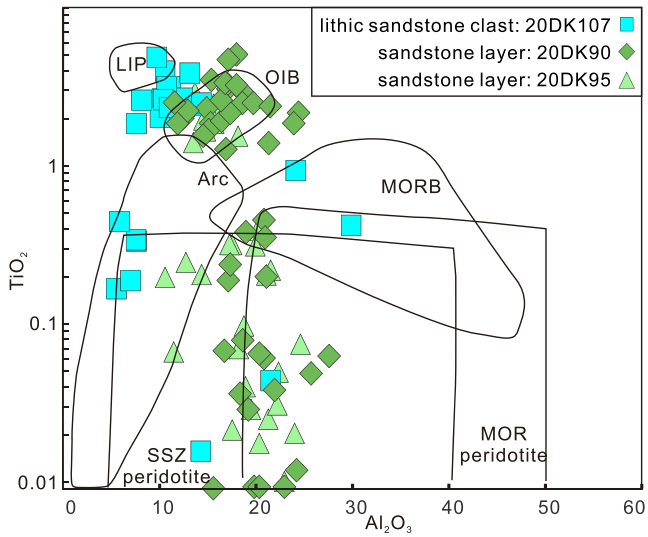

Figure 7. TiO_2 versus Al_2O_3 tectonic discrimination diagram of the detrital chromian spinels, with fields modified from Kamenetsky et al. (2001). LIP, large igneous province; OIB, oceanic-island basalt; MORB, mid-oceanic ridge basalt; SSZ, supra-subduction zone; MOR, mid-oceanic ridge.

sandstone with some phyllite and metamorphic sandstone, interlayered with Middle Jurassic (166–160 Ma) volcanic rocks (S.-M. Li et al., 2020; X. Li et al., 2015; D.-C. Zhu et al., 2016). These sandstones are quartzo-lithic to litho-quartzose in composition and were sourced from the Qiangtang terrane based on their similar detrital zircon U-Pb age distribution (Figure S6 in Supporting Information S1; S.-M. Li et al., 2020). In contrast, the Jienu Group in the Jienu Mountain region consists of conglomerate and sandstone fed by multiple potential sources, with no interlayered volcanics (only clasts). Therefore, the Jienu Group from the Jienu Mountain region (where the Jienu Group was first defined) should not be simply correlated with that in the Dongqiao-Beila region, and its depositional age should be re-evaluated.

Our dating of basaltic andesite clasts in conglomerates gives a robust age constraint, suggesting the Jienu Group should be broadly contemporaneous or slightly younger than ca. 147 Ma. In contrast, the youngest detrital zircon ages from the two sandstone samples (20DK90 and 20DK95) only provide much looser constraints. Sample 20DK90 contains only a single Jurassic zircon at 171 ± 6 Ma, with others between 224 and 2642 Ma. The youngest four Jurassic zircon grains within 20DK95 are of 164, 168, 169 and 170 Ma U-Pb ages, respectively. The quartz sandstone clast (sample 20DK108 and 20DK100) and lithic sandstone clast (20DK107) in the Jienu Group yield single youngest zircon U-Pb ages of 414 ± 8 Ma and 214 ± 6 Ma, respectively, which cannot provide useful constraints on the depositional age for the Jienu Group.

If the Jienu Group was deposited as late as late Early Cretaceous, then syn-depositional detrital zircons can potentially be found. This is because the Eshaerbu, Duoba and Duoni formations, deposited in the adjacent marine basin of northern Lhasa are Aptian–Albian in age (~122–110 Ma) based on dating of tuffs and youngest detrital zircon ages, and all contain predominantly Early Cretaceous detrital zircons (Lai et al., 2019; Leier, DeCelles, et al., 2007; Q.-H. Zhang et al., 2011) (Figure S7 in Supporting Information S1). Therefore, we suggest the

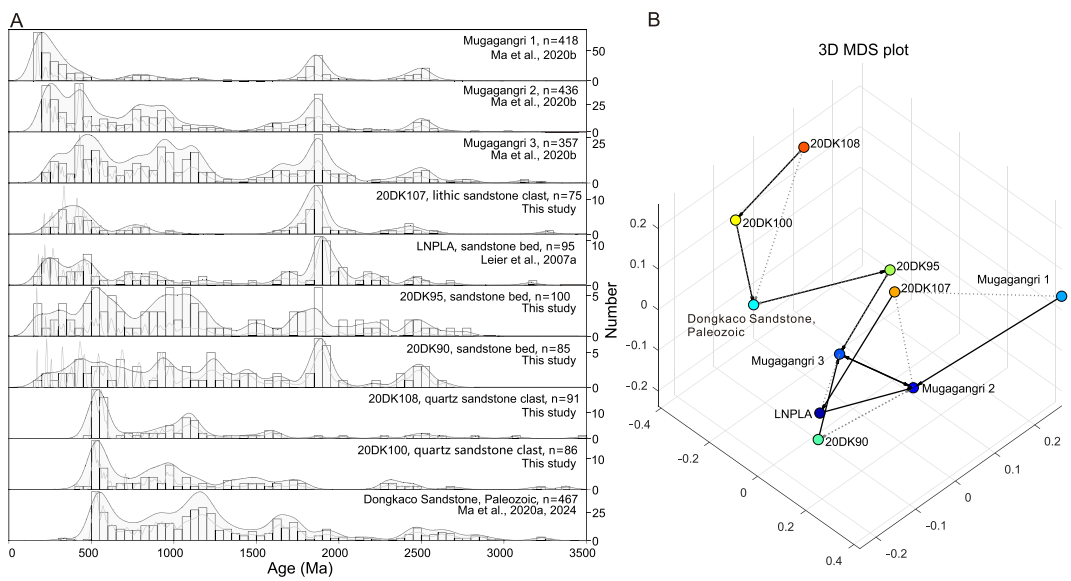

Figure 8. Provenance inferred from detrital zircon U-Pb age data. (a) Detrital zircon U-Pb age spectra from sandstone horizons and clasts in the Jienu Group, presented as kernel density estimates (filled), probability density (gray curve), and histograms (bin width 50 Ma). (b) Three-dimensional (3-D) multidimensional scaling (MDS) results for the detrital zircon U-Pb age spectra (likeness was used as the basis for comparison, and metric squared stress as the criterion, with a stress of 0.15382). Black and gray arrows point from each sample to its closest and second closest neighbors (the sample most similar to it based on the selected matrix), respectively.

depositional age of the Jienu Group falls within the range of 147 to 122 Ma, making it younger than the volcanic clast ages but older than the late Early Cretaceous deposits.

5.2. Source-to-Sink Reconstruction

The southwards-fining trend in grain size from north (Jienu Mountain section) to south (the south Jienu Mountain and Yilai sections and the Erusongduo site) suggests a transition from proximal to distal submarine fan, aligning with depositional modes of gravel-rich submarine fans summarized from many modern and ancient field examples (Reading & Richards, 1994). If this interpretation is valid, it also indicates a provenance from the north. In addition, the olistostrome in the Jienu Mountain and south Jienu Mountain sections suggests deposition in a very proximal setting, typically tectonically-controlled and close to submarine fault scarps (Ferentinos et al., 1988; Surlyk, 1978). The Qiangtang terrane and subduction complex may serve as the source area to the north of the basin as they were tectonically active during the Middle to Late Jurassic (A. Ma et al., 2018, 2023; A. Ma, Hu, Kapp, Lai, et al., 2020).

Compositionally mature quartzose sandstone, mostly deposited on passive continental margins (Cawood et al., 2012; Garzanti et al., 2018), is an important clast type in the upper unit of the Jienu Group. Regionally, potential sources of quartzose sandstone are Paleozoic in age and were deposited in northern and central Lhasa (Leier, Kapp, et al., 2007; Q. Wang et al., 2021) and on the Dongkaco microcontinent (Girardeau et al., 1984; Ma, Hu, Kapp, BouDagher-Fadel, & Lai, 2020). As the available evidence indicates provenance from the north, the Lhasa terrane is excluded as a potential source. The Dongkaco microcontinent is thus likely the unique source for the quartzose sandstone fragments in the Jienu Group, and this is supported by the highly similar detrital zircon U-Pb age spectra in the quartzose sandstone clasts and the Paleozoic strata of the Dongkaco microcontinent, as shown on a MDS diagram (Figure 8b).

The lithic sandstone clasts in the Jienu Group are probably sourced from a subduction complex related to the northward subduction along the northern branch of the Bangong-Nujiang suture zone. This subduction complex contains three groups of sandstone with distinct provenance signals (Ma, Hu, Kapp, Lai, et al., 2020). The subduction complex rocks were obducted over the Dongkaco microcontinent in the Late Jurassic together with the Dongqiao ophiolite (Ma, Hu, Kapp, BouDagher-Fadel, & Lai, 2020). The similar detrital zircon U-Pb age spectra of the lithic sandstone clasts and the Mugagangri Complex (Figure 8a) support this interpretation.

The mafic volcanic rock clasts in the Jienu Group indicate provenance from both seamount(s) and arc(s). The OIB fragments are likely sourced from accreted seamount fragments in the obducted subduction complex. A large number of seamount remnants of different ages have been reported within the Bangong-Nujiang suture zone (J.-J. Fan et al., 2018, 2024; Z. Wang et al., 2005), which suggests that oceanic intraplate magmatism was widespread and thus OIB fragments would be expected in the basins sourced from subduction complex. The ca. 147 Ma arc-like basalts and basaltic andesite are mostly likely sourced from the magmatic arc in the southmost Qiangtang terrane and within the Dongqiao suture which have been reported in Kangqiong (Y. Li et al., 2016; Yang et al., 2021) and Gaaco (A. Ma et al., 2018). The detrital Cr-Spinel data from the Jienu Group sandstones support seamount and volcanic arc sources, along with an additional contribution from a supra-subduction zone ophiolite which likely represents the obducted Dongqiao ophiolite. The fossiliferous shallow marine limestone clasts were likely sourced either from a carbonate platform fringing seamount(s) or the Late Jurassic Shamuluo Formation in southmost Qiangtang (A. Ma et al., 2018).

As felsic crustal rocks (and sedimentary rocks derived from them) have higher zircon fertility than mafic rocks (Chew et al., 2020; Malusà et al., 2016; Spencer et al., 2018), the potential sources of zircons in the Jienu Group sandstone should mainly include the Paleozoic sedimentary rocks of the Dongkaco microcontinent (Ma, Hu, Kapp, BouDagher-Fadel, & Lai, 2020) and the subduction complex (Mugagangri Complex) in the north branch of Bangong-Nujiang suture zone which was obducted over the Dongkaco microcontinent during the Late Jurassic (Girardeau et al., 1984; Ma, Hu, Kapp, Lai, et al., 2020). Forward mixture modeling based on detrital zircon U-Pb geochronology is applied to calculate the relative contributions of the Paleozoic sedimentary rocks and the three groups of sandstone within the Mugagangri Complex, which are synthesized as four parents (Malkowski et al., 2019, 2022; Saylor & Sundell, 2016; Saylor et al., 2019; Sharman & Johnstone, 2017). Two quartzose sandstone clasts (20DK100 and 20DK108) from the Jienu Group are grouped into the Dongqiao microcontinent and lithic sandstone clast 20DK107 is placed into Group 2 of the Mugagangri Complex. The child samples include four sandstone samples, three from this study (20DK90, 20DK95) and sample LNPLA from Leier,

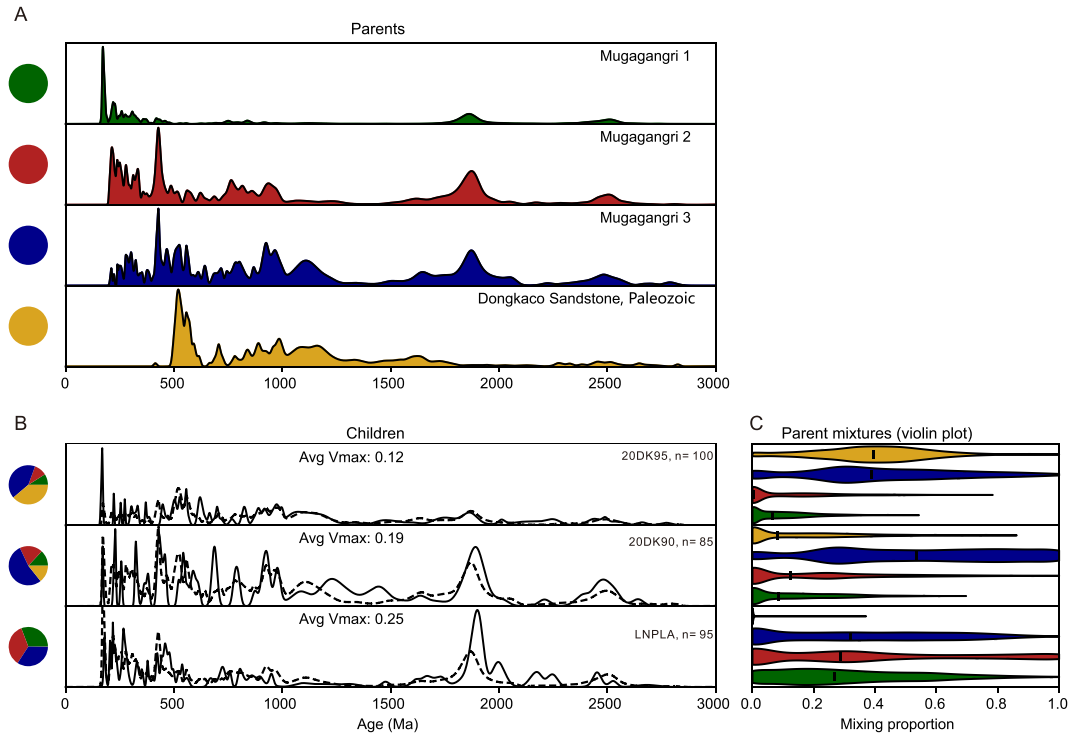

Figure 9. Forward mixture modeling of relative provenance contributions from regional potential sources based on detrital zircon U-Pb age spectra. (a) Age PDP spectrum curves for four potential sources. (b) Four-source forward mixture modeling results for three samples from the Jienu Group as child distributions using the Vmax comparison metric. The dashed line represents the bootstrapped (5,000 iterations) best-fit age spectrum distribution, while the solid line represents the actual age spectrum. The pie chart on the left represents the best-fit mixture proportions for the different sources. (c) Violin plots displaying best-fit contribution and the range of uncertainty for each parent contribution. The distribution range is between 2.5% and 97.5% of the mixtures.

DeCelles, et al. (2007). Sample LNPLA from the Jienu Group adjacent to the Yilai section yields less 500–1300 Ma zircons compared to those to the north, with three main peaks at 1900, 460 and 200–300 Ma and minor peaks at 1700, 2200, and 2470 Ma, which show an affinity with the obducted subduction complex and lithic sandstone clasts in the MDS plot (Figure 8b).

Forward mixture modeling of source contributions estimates that the Dongkaco microcontinent is absent (0%) for the southernmost sample LNPLA (Table S11 in Supporting Information S2; Figure 9). Conversely, the Mugagangri subduction complex contributed nearly 100% of the zircon detritus to sample LNPLA (Figure 9). However, the high Vmax value (0.25) suggests that the modeling result does not fit perfectly with the observed age distribution (Figure 9). The two sandstones from the Jienu Mountain section (20DK90 and 20DK95) yield varying contributions from both the obducted subduction complex and the Dongkaco microcontinent, with the latter accounting for 14% and 39%, respectively (Figure 9).

5.3. Lhasa-Qiangtang Continental Collision and the Role of Microcontinents

The latest Jurassic to Early Cretaceous (147–122 Ma) depositional age and mixed provenance signals of the Jienu Group within the Bangong-Nujiang suture zone require a two-stage collision between the Lhasa and Qiangtang terranes. The first collision between the Dongkaco microcontinent and the Qiangtang terrane along the Dongqiao suture zone took place during the late Middle Jurassic to Late Jurassic, as shown by Dongqiao ophiolite obduction and deposition of the synorogenic Biluoco, Shamuluo and Dongqiao formations from south Qiangtang to the Dongqiao suture zone (A. Ma et al., 2017, 2018; A. Ma, Hu, Kapp, BouDagher-Fadel, & Lai, 2020). The second collision between the Lhasa terrane and the Dongkaco microcontinent (i.e., final collision between Lhasa and Qiangtang) occurred during the latest Jurassic to Early Cretaceous (148–122 Ma) (Figure 10).

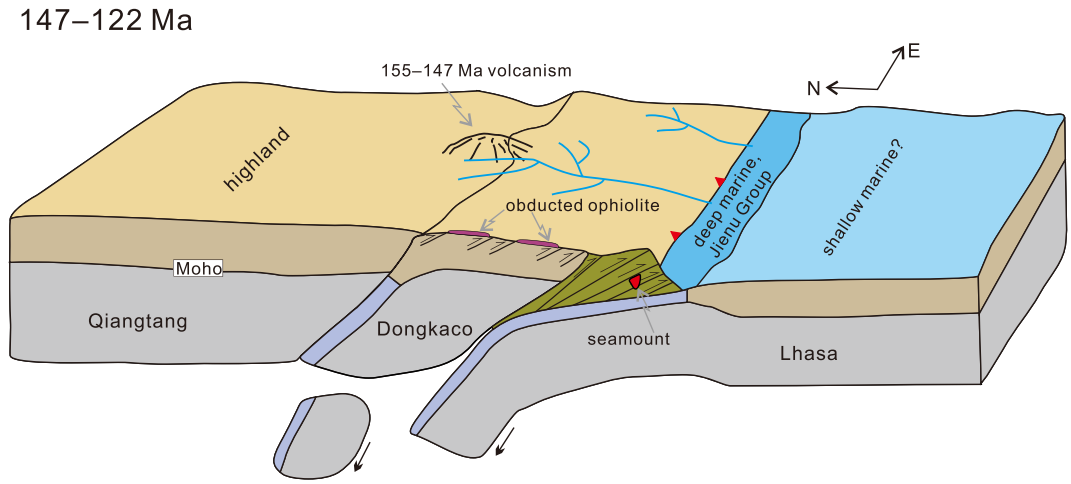

Figure 10. Tectonic model illustrating the latest Jurassic to Early Cretaceous tectonic setting and depositional environment of the Jienu Group during the final Lhasa-Qiangtang collision.

We suggest the Dongkaco and Lhasa collision caused reactivation of the obducted thrust sheet including the ophiolite, subduction complex, and the quartzose sandstone strata of the Dongkaco microcontinent, which served as the provenance for the studied Jienu Group. Three lines of evidence support the Jienu Group was deposited in a syn-collisional trench basin between the Dongkaco microcontinent and Lhasa terrane. First, the Jienu Group was deposited in a deep marine environment and the existence of debris- and blocky-flows related olistostromes was likely indicative of activation of thrust belts bounding the basin (Festa et al., 2016). Second, the Jienu Group deposition occurred in a basin between the Dongkaco microcontinent and the Lhasa terrane. Third, the Jienu Group deposition was bounded by and also sourced from the subduction complex and sutured Dongkaco microcontinent to the north. We therefore suggest that the arrival of the continental margin of the Lhasa terrane into the north-dipping subduction zone was the most likely trigger for deposition of the Jienu Group in a syn-collisional trench basin.

The syn-collisional trench basin was believed to be equivalent to a foredeep in the earliest stages of a peripheral foreland basin system (DeCelles & Giles, 1996; DeCelles et al., 2014). However, it has been noted that foreland basin systems and pervasive orogeny do not usually form in the early stage of continental collision, and thus the syn-collisional trench basin instead of foredeep is more suitable to be adopted (An et al., 2021; X. Hu et al., 2020; Q. Liu et al., 2021). During latest Jurassic to Early Cretaceous time when the Jienu Group was deposited, northern Lhasa was covered by a shallow sea carbonate platform of the Rila Formation (Q.-H. Zhang et al., 2011). Both the syn-collisional trench basin and northern Lhasa would later be incorporated into foreland thrust belts and the foredeep would migrate toward the lower plate, as in reconstructions of the Himalayan foreland basin (DeCelles et al., 2014). Such basin evolution is supported by the discovery of younger deep-marine foredeep deposition (Eshaerbu Formation) of Early Cretaceous age in northern Lhasa (Lai et al., 2019; Q.-H. Zhang et al., 2011).

An alternative model involves seamount collision, as remnants of Triassic to earliest Cretaceous seamounts were reported in the Bangong-Nujiang suture zone (J.-J. Fan et al., 2024) and seamount fragments are present as detritus within the Jienu Group. However, seamounts of significant size are not found in the region between the Dongkaco microcontinent and the Lhasa terrane. The Tarenben seamount (Figure 1c), as the largest seamount nearby, developed within the Dongqiao oceanic branch to the north of Dongkaco microcontinent during the Late Triassic to Late Jurassic (J.-J. Fan et al., 2024; Z. Wang et al., 2005), and thus cannot have caused the collision within the Beila Ocean to its south.

The identification of Early Jurassic and Early Cretaceous oceanic plateau fragments within the Bangong-Nujiang suture zone (Yan & Zhang, 2020; K.-J. Zhang et al., 2014; W.-Q. Zhang et al., 2021) may support an oceanic plateau collision model. Collision with an oceanic plateau would result in the delivery of oceanic plateau-derived detritus to syn-orogenic basins (Andjić et al., 2019). However, the OIB basalt clasts in the Jienu Group, with LREE-enriched chondrite-normalized REE patterns (Figure 6a), are characteristic of oceanic islands, as opposed to oceanic plateaus which yield predominantly flat REE patterns (Kerr, 2014). Additionally, it is unknown if the

reported basaltic rocks formed a plateau of a large extent as they are somewhat scattered in separate areas within the Bangong-Nujiang suture zone.

Along strike to the west, the Dongkaco microcontinent becomes progressively narrower and is not seen northwest of Selinco (Figure 1b). Therefore, to the northwest of the Selinco, there may have instead been a direct collision between Lhasa and Qiangtang, or the microcontinent was present but fully subducted. Further west in the Gaize region, there is no evidence to date for the presence of a microcontinent. In contrast to the trench basin in the Jienu Mountain region, the latest Middle Jurassic syn-collisional trench basin in the Gaize region recorded recycled detritus from an accretionary prism and forearc basin, with abundant syn-depositional zircons (G. Sun et al., 2019).

Limited adakite magmatism at ca. 150 Ma can be traced along the southern margin of Qiangtang and Bangong-Nujiang suture zone from Gaize in the west (S.-M. Li et al., 2016) to the Dongqiao in the east. We interpret this magmatism as related to the break-off of the subducted Dongqiao oceanic slab, as documented in many other orogenic belts (L. Ma et al., 2014; Yousefi & Lentz, 2024) and predicted by numerical modeling (Freeburn et al., 2017). Though the Ti-in-zircon temperature of the adakite melts (mean of ca. 737°C based on zircons from sample 21QM95) is indistinguishable with the zircon saturation temperature of the Kangqiong adakites (694–742°C, Yang et al., 2021), neither models of subduction erosion (Yang et al., 2021) nor active ridge-trench interaction (S.-M. Li et al., 2020; Y. Li et al., 2016) are applicable in the Lunpola-Jienu Mountain region. This is because the suturing of the Dongkaco microcontinent with the Qiangtang terrane had terminated the subduction of Dongqiao oceanic lithosphere by the Late Jurassic (A. Ma et al., 2023). In addition, even if subduction erosion or ridge subduction of the Beila Ocean occurred, these processes would have been geographically too distal to generate the adakite magmatism observed north of the Dongkaco microcontinent.

5.4. Implications for the Development of the Cenozoic Bangong-Nujiang Suture Zone Basins

Our model of the two-stage collision in the Bangong-Nujiang suture zone is important for the understanding of the mechanisms and evolution of the subsequent uplift of central Tibet. First, deep marine environments in the Jienu Mountain region persisted into latest Jurassic to Early Cretaceous time, which places the earliest limit for the uplift of the Bangong-Nujiang suture zone. This age is younger than previously suggested based on the Triassic to Late Jurassic Tarenben oceanic island (J.-J. Fan et al., 2024; Z. Wang et al., 2005) and the Late Jurassic remnant shallow marine deposition of the Shamuluo Formation to the north of the Lunpola basin (A. Ma et al., 2018). The Bangong-Nujiang suture zone became subaerially exposed during the Aptian to Albian, as suggested by deposition of continental red beds (Y. Hu et al., 2020; Z. Zhu et al., 2019). At the same time, the siliciclastic materials eroded from Qiangtang and Bangong-Nujiang suture zone rocks could have bypassed the Jienu Mountain region and been deposited in the northern Lhasa shallow marine basin (Lai et al., 2019; Xu et al., 2022). The Late Cretaceous surface evolution of the Lunpola-Jienu Mountain region is uncertain as it was a period of non-deposition, but the Lunpola basin likely started subsiding in the early Cenozoic (Z. Han et al., 2019; Xiong et al., 2022). The reactivation of older structures may have contributed to basin initiation, though no evidence has been documented so far.

Second, the two-stage collision that led to the incorporation of the Dongkaco microcontinent may have resulted in a relatively rigid and stable basement for the development of the Lunpola basin in the Cenozoic. This may explain why the Lunpola basin is wide and dominated by widespread lacustrine deposition, and experienced relatively constant deposition through the Paleocene to the Miocene. In contrast, the sedimentary facies in the Nima, Gaize, and Awenco basins, where no microcontinent basement has been documented, either exhibit abrupt facies changes with time (e.g., the Nima Basin) (DeCelles et al., 2007) or were confined to narrower regions (the Gaize and Awenco basins) (X. Han et al., 2022; Song et al., 2023; L. Wang et al., 2011; Wei et al., 2016).

6. Conclusions

The newly discovered deep-marine gravity-fan succession in the Bangong-Nujiang suture zone was deposited in a syn-collisional trench during the latest Jurassic to Early Cretaceous. This unit yields multiple provenance signals indicating sources from an obducted subduction complex and ophiolite, the Dongkaco microcontinent, and broadly contemporaneous volcanic arc rocks. The deposition was related to the final collision between the Lhasa terrane and the already assembled Dongkaco-Qiangtang terranes. Incorporation of the Dongkaco microcontinent into the Bangong-Nujiang suture zone explains why the Lunpola basin, with the Dongkaco microcontinent as its

basement, is the widest Cenozoic basin along the suture zone and highlights the importance of Mesozoic tectonic inheritance on subsequent Cenozoic uplift of the Tibetan Plateau.

Data Availability Statement

The data set (A. Ma et al., 2025) supporting this research is provided in the Supporting Information and can also be accessed via Figshare, an open-access online repository, at https://doi.org/10.6084/m9.figshare.26172568.

Acknowledgments
We thank Weiwei Xue and Youzhe Jibu for their help in the field. We are grateful to Dr. Taylor Schildgen and Dr. Majie Fan for handling our submission, and to Dr. Majie Fan and the two anonymous reviewers for their comments. This study was supported by the National Natural Science Foundation of China (Grant 42472161), the Project of Deep Earth Exploration and Mineral Resource Prospecting, National Science and Technology Major Project of China (No. 2024ZD1001103), China Postdoctoral Science Foundation—Special Program (2024T170395), and the Jiangsu Funding Program for Excellent Postdoctoral Talent (2022ZB14). David Chew acknowledges support from Research Ireland through research Grant 13/RC/2092_P2 (iCRAG Research Centre).

References

An, W., Hu, X., Garzanti, E., Wang, J. G., & Liu, Q. (2021). New precise dating of the India-Asia collision in the Tibetan Himalaya at 61 Ma. *Geophysical Research Letters*, *48*(3), e2020GL090641. https://doi.org/10.1029/2020GL090641

Andjić, G., Baumgartner, P. O., & Baumgartner-Mora, C. (2019). Collision of the Caribbean Large Igneous Province with the Americas: Earliest evidence from the forearc of Costa Rica. *GSA Bulletin*, *131*(9–10), 1555–1580. https://doi.org/10.1130/B35037.1

Black, L., & Gulson, B. (1978). The age of the Mud Tank Carbonatite, Strangways Range, Northern Territory. *Journal of Australian Geology and Geophysics*, *3*, 227–232.

Cawood, P. A., Hawkesworth, C. J., & Dhuime, B. (2012). Detrital zircon record and tectonic setting. *Geology*, *40*(10), 875–878. https://doi.org/10.1130/g32945.1

Chen, Y., Chen, G., Zhang, K., Zhao, S., Liu, B., & Suolang, G. (2002). *Geological Report of the 1:250, 000 Regional Geological Survey in Baingoin Area* (in Chinese). Geological Publishing House.

Chew, D., O'Sullivan, G., Caracciolo, L., Mark, C., & Tyrrell, S. (2020). Sourcing the sand: Accessory mineral fertility, analytical and other biases in detrital U-Pb provenance analysis. *Earth-Science Reviews*, *202*, 103093. https://doi.org/10.1016/j.earscirev.2020.103093

Chew, D., Petrus, J., & Kamber, B. (2014). U–Pb LA–ICPMS dating using accessory mineral standards with variable common Pb. *Chemical Geology*, *363*, 185–199. https://doi.org/10.1016/j.chemgeo.2013.11.006

Chew, D., Sylvester, P. J., & Tubrett, M. N. (2011). U–Pb and Th–Pb dating of apatite by LA-ICPMS. *Chemical Geology*, *280*(1–2), 200–216. https://doi.org/10.1016/j.chemgeo.2010.11.010

Cookenboo, H., Bustin, R., & Wilks, K. (1997). Detrital chromian spinel compositions used to reconstruct the tectonic setting of provenance; implications for orogeny in the Canadian Cordillera. *Journal of Sedimentary Research*, *67*(1), 116–123. https://doi.org/10.1306/D4268509-2B26-11D7-8648000102C1865D

DeCelles, P. G., & Giles, K. A. (1996). Foreland basin systems. *Basin Research*, *8*(2), 105–123. https://doi.org/10.1046/j.1365-2117.1996.01491.x

DeCelles, P. G., Kapp, P., Ding, L., & Gehrels, G. (2007). Late Cretaceous to middle Tertiary basin evolution in the central Tibetan Plateau: Changing environments in response to tectonic partitioning, aridification, and regional elevation gain. *Geological Society of America Bulletin*, *119*(5–6), 654–680. https://doi.org/10.1130/B26074.1

DeCelles, P. G., Kapp, P., Gehrels, G. E., & Ding, L. (2014). Paleocene-Eocene foreland basin evolution in the Himalaya of southern Tibet and Nepal: Implications for the age of initial India-Asia collision. *Tectonics*, *33*(5), 824–849. https://doi.org/10.1002/2014TC003522

Dewey, J. F., Shackleton, R. M., Chang, C., & Sun, Y. (1988). The tectonic evolution of the Tibetan Plateau. *Philosophical Transactions of the Royal Society of London A: Mathematical, Physical and Engineering Sciences*, *327*(1594), 379–413. https://doi.org/10.1098/rsta.1988.0135

Ding, L., Kapp, P., Cai, F., Garzione, C. N., Xiong, Z., Wang, H., & Wang, C. (2022). Timing and mechanisms of Tibetan Plateau uplift. *Nature Reviews Earth & Environment*, *3*(10), 1–16. https://doi.org/10.1038/s43017-022-00318-4

Drummond, M., Defant, M., & Kepezhinskas, P. (1996). Petrogenesis of slab-derived trondhjemite–tonalite–dacite/adakite magmas. *Earth and Environmental Science Transactions of The Royal Society of Edinburgh*, *87*(1–2), 205–215. https://doi.org/10.1017/S0263593300006611

Fan, J.-J., Li, C., Liu, J.-H., Wang, M., Liu, Y.-M., & Xie, C.-M. (2018). The Middle Triassic evolution of the Bangong–Nujiang Tethyan Ocean: Evidence from analyses of OIB-type basalts and OIB-derived phonolites in northern Tibet. *International Journal of Earth Sciences*, *107*(5), 1755–1775. https://doi.org/10.1007/s00531-017-1570-x

Fan, J.-J., Zhang, B.-C., Niu, Y., Luo, A.-B., & Hao, Y.-J. (2024). Resolving the nature and evolution of the Bangong–Nujiang Tethyan Ocean: New perspectives from the intraplate oceanic-island fragments preserved in Northern Tibet. *Bulletin*, *136*(3–4), 1379–1394. https://doi.org/10.1130/B37044.1

Fan, S., Ding, L., Murphy, M. A., Yao, W., & Yin, A. (2017). Late Paleozoic and Mesozoic evolution of the Lhasa Terrane in the Xainza area of southern Tibet. *Tectonophysics*, *721*, 415–434. https://doi.org/10.1016/j.tecto.2017.10.022

Farnsworth, A., Valdes, P. J., Ding, L., Spicer, R. A., Li, S.-H., Su, T., et al. (2023). Limits of oxygen isotope palaeoaltimetry in Tibet. *Earth and Planetary Science Letters*, *606*, 118040. https://doi.org/10.1016/j.epsl.2023.118040

Ferentinos, G., Papatheodorou, G., & Collins, M. (1988). Sediment transport processes on an active submarine fault escarpment: Gulf of Corinth, Greece. *Marine Geology*, *83*(1–4), 43–61. https://doi.org/10.1016/0025-3227(88)90051-5

Festa, A., Ogata, K., Pini, G. A., Dilek, Y., & Alonso, J. L. (2016). Origin and significance of olistostromes in the evolution of orogenic belts: A global synthesis. *Gondwana Research*, *39*, 180–203. https://doi.org/10.1016/j.gr.2016.08.002

Freeburn, R., Bouilhol, P., Maunder, B., Magni, V., & van Hunen, J. (2017). Numerical models of the magmatic processes induced by slab breakoff. *Earth and Planetary Science Letters*, *478*, 203–213. https://doi.org/10.1016/j.epsl.2017.09.008

Garzanti, E. (2019). Petrographic classification of sand and sandstone. *Earth-Science Reviews*, *192*, 545–563. https://doi.org/10.1016/j.earscirev.2018.12.014

Garzanti, E., Dinis, P., Vermeesch, P., Andò, S., Hahn, A., Huvi, J., et al. (2018). Dynamic uplift, recycling, and climate control on the petrology of passive-margin sand (Angola). *Sedimentary Geology*, *375*, 86–104. https://doi.org/10.1016/j.sedgeo.2017.12.009

Girardeau, J., Marcoux, J., Allegre, C. J., Bassoullet, J. P., Tang, Y. K., Xiao, X. C., et al. (1984). Tectonic environment and geodynamic significance of the Neo-Cimmerian Donqiao ophiolite, Bangong-Nujiang suture zone, Tibet. *Nature*, *307*(5946), 27–31. https://doi.org/10.1038/307027a0

Guynn, J., Kapp, P., Gehrels, G. E., & Ding, L. (2012). U–Pb geochronology of basement rocks in central Tibet and paleogeographic implications. *Journal of Asian Earth Sciences*, *43*(1), 23–50. https://doi.org/10.1016/j.jseaes.2011.09.003

Guynn, J., Kapp, P., Pullen, A., Heizler, M., Gehrels, G., & Ding, L. (2006). Tibetan basement rocks near Amdo reveal "missing" Mesozoic tectonism along the Bangong suture, central Tibet. *Geology*, *34*(6), 505–508. https://doi.org/10.1130/G22453.1

Han, X., Dai, J.-G., Lin, J., Xu, S., Liu, B., Hu, T., et al. (2022). An Oligocene-Miocene intermontane narrow lowland in the central Tibetan Plateau: Insights from provenance analysis and palynological record of a Cenozoic sedimentary succession. *Journal of Asian Earth Sciences*, *240*, 105438. https://doi.org/10.1016/j.jseaes.2022.105438

Han, Z., Sinclair, H. D., Li, Y., Wang, C., Tao, Z., Qian, X., et al. (2019). Internal drainage has sustained low-relief Tibetan landscapes since the early Miocene. *Geophysical Research Letters*, *46*(15), 8741–8752. https://doi.org/10.1029/2019GL083019

Hu, X., An, W., Garzanti, E., & Liu, Q. (2020). Recognition of trench basins in collisional orogens: Insights from the Yarlung Zangbo suture zone in southern Tibet. *Science China Earth Sciences*, *63*(12), 2017–2028. https://doi.org/10.1007/s11430-019-9687-x

Hu, X.-M., An, W., Wang, J.-G., Garzanti, E., & Guo, R.-H. (2014). Himalayan detrital chromian spinels and timing of Indus-Yarlung ophiolite erosion. *Tectonophysics*, *621*, 60–68. https://doi.org/10.1016/j.tecto.2014.02.003

Hu, X.-M., Ma, A.-L., Xue, W.-W., Garzanti, E., Cao, Y., Li, S.-M., et al. (2022). Exploring a lost ocean in the Tibetan Plateau: Birth, growth, and demise of the Bangong-Nujiang Ocean. *Earth-Science Reviews*, *229*, 104031. https://doi.org/10.1016/j.earscirev.2022.104031

Hu, Y., Liu, Z. B., Wang, G., Gao, J., Song, Y., Zheng, M., & Li, D. (2020). Study of molasse within the middle segment of the Bangong-Nujiang suture zone, central Tibet: Constraints of ocean–continent transform. *Geological Journal*, *55*(10), 6625–6641. https://doi.org/10.1002/gj.3832

Ingersoll, R. V., Bullard, T. F., Ford, R. L., Grimm, J. P., Pickle, J. D., & Sares, S. W. (1984). The effect of grain size on detrital modes: A test of the Gazzi-Dickinson point-counting method. *Journal of Sedimentary Research*, *54*(1), 103–116. https://doi.org/10.1306/212F8783-2B24-11D7-8648000102C1865D

Jackson, S. E., Pearson, N. J., Griffin, W. L., & Belousova, E. A. (2004). The application of laser ablation-inductively coupled plasma-mass spectrometry to in situ U–Pb zircon geochronology. *Chemical Geology*, *211*(1–2), 47–69. https://doi.org/10.1016/j.chemgeo.2004.06.017

Kamenetsky, V. S., Crawford, A. J., & Meffre, S. (2001). Factors controlling chemistry of magmatic spinel: An empirical study of associated olivine, Cr-spinel and melt inclusions from primitive rocks. *Journal of Petrology*, *42*(4), 655–671. https://doi.org/10.1093/petrology/42.4.655

Kapp, P., & DeCelles, P. G. (2019). Mesozoic–Cenozoic geological evolution of the Himalayan-Tibetan orogen and working tectonic hypotheses. *American Journal of Science*, *319*(3), 159–254. https://doi.org/10.2475/03.2019.01

Kerr, A. C. (2014). Oceanic plateaus. *Treatise on Geochemistry*, *3*, 537–565. https://doi.org/10.1016/B0-08-043751-6/03033-4

Kuiper, N. H. (1960). Tests concerning random points on a circle. In *Paper presented at Koninklijke Nederlandse Akademie van Wetenschappen, Series A*.

Lai, W., Hu, X., Garzanti, E., Xu, Y., Ma, A., & Li, W. (2019). Early Cretaceous sedimentary evolution of the northern Lhasa terrane and the timing of initial Lhasa-Qiangtang collision. *Gondwana Research*, *73*, 136–152. https://doi.org/10.1016/j.gr.2019.03.016

Leier, A. L., DeCelles, P. G., Kapp, P., & Gehrels, G. E. (2007). Lower Cretaceous strata in the Lhasa Terrane, Tibet, with implications for understanding the early tectonic history of the Tibetan Plateau. *Journal of Sedimentary Research*, *77*(10), 809–825. https://doi.org/10.2110/jsr.2007.078

Leier, A. L., Kapp, P., Gehrels, G. E., & DeCelles, P. G. (2007). Detrital zircon geochronology of Carboniferous–Cretaceous strata in the Lhasa terrane, Southern Tibet. *Basin Research*, *19*(3), 361–378. https://doi.org/10.1111/j.1365-2117.2007.00330.x

Li, L., Garzione, C. N., Lu, H., & Quade, J. (2024). Neogene surface uplift of the Lunpola Basin in Central Tibet: Implications for uplifting and flattening of orogenic plateaus. *Earth and Planetary Science Letters*, *646*, 118961. https://doi.org/10.1016/j.epsl.2024.118961

Li, L., Lu, H., Garzione, C., & Fan, M. (2022). Cenozoic paleoelevation history of the Lunpola Basin in Central Tibet: New evidence from volcanic glass hydrogen isotopes and a critical review. *Earth-Science Reviews*, *231*, 104068. https://doi.org/10.1016/j.earscirev.2022.104068

Li, S., Yin, C.-Q., Guilmette, C., Ding, L., & Zhang, J. (2019). Birth and demise of the Bangong-Nujiang Tethyan Ocean: A review from the Gerze area of central Tibet. *Earth-Science Reviews*, *198*, 102907. https://doi.org/10.1016/j.earscirev.2019.102907

Li, S.-M., Wang, Q., Zhu, D.-C., Cawood, P. A., Stern, R. J., Weinberg, R., et al. (2020). Reconciling orogenic drivers for the evolution of the Bangong-Nujiang Tethys during Middle-Late Jurassic. *Tectonics*, *39*(2), e2019TC005951. https://doi.org/10.1029/2019TC005951

Li, S.-M., Zhu, D. C., Wang, Q., Zhao, Z., Zhang, L. L., Liu, S. A., et al. (2016). Slab-derived adakites and subslab asthenosphere-derived OIB-type rocks at 156 ± 2 Ma from the north of Gerze, central Tibet: Records of the Bangong–Nujiang oceanic ridge subduction during the Late Jurassic. *Lithos*, *262*, 456–469. https://doi.org/10.1016/j.lithos.2016.07.029

Li, X., Wang, B., Liu, H., Wang, L., & Chen, L. (2015). The Late Jurassic high-Mg andesites in the Daru Tso area, Tibet: Evidence for the subduction of the Bangong Co-Nujiang River oceanic lithosphere (in Chinese with English abstract). *Geological Bulletin of China*, *34*(2/3), 251–261.

Li, Y., He, J., Han, Z., Wang, C., Ma, P., Zhou, A., et al. (2016). Late Jurassic sodium-rich adakitic intrusive rocks in the southern Qiangtang terrane, central Tibet, and their implications for the Bangong–Nujiang Ocean subduction. *Lithos*, *245*, 34–46. https://doi.org/10.1016/j.lithos.2015.10.014

Liu, Q., Kneller, B., An, W., & Hu, X. (2021). Sedimentological responses to initial continental collision: Triggering of sand injection and onset of mass movement in a syn-collisional trench basin, Saga, southern Tibet. *Journal of the Geological Society*, *178*(6), jgs2020-2178. https://doi.org/10.1144/jgs2020-178

Liu, Y., Hu, Z., Zong, K., Gao, C., Gao, S., Xu, J., & Chen, H. (2010). Reappraisement and refinement of zircon U-Pb isotope and trace element analyses by LA-ICP-MS. *Chinese Science Bulletin*, *55*(15), 1535–1546. https://doi.org/10.1007/s11434-010-3052-4

Ludwig, K. R. (2011). *Isoplot/Ex, Version 4.15: A geochronological toolkit for Microsoft Excel*. Geochronology Center Berkeley, v. 4.

Ma, A., Hu, X., Chew, D., Liang, W., Wen, D., & Deng, T. (2025). A latest Jurassic to Early Cretaceous syn-collisional trench sequence in central Tibet recorded the role of microcontinents in Lhasa–Qiangtang collision - Supporting Information [Dataset]. *Figshare*. https://doi.org/10.6084/m9.figshare.26172568

Ma, A., Hu, X., Garzanti, E., Boudagher-Fadel, M., Xue, W., Han, Z., & Wang, P. (2023). Paleogeographic and tectonic evolution of Mesozoic Qiangtang basins (Tibet). *Tectonophysics*, *862*, 229957. https://doi.org/10.1016/j.tecto.2023.229957

Ma, A., Hu, X., Garzanti, E., Xue, W., Schlagintweit, F., Xu, Y., & Lai, W. (2024). Diachronous Cretaceous closure of the Bangong-Nujiang-Shyok Ocean (westernmost central Tibet). *Tectonics*, *43*(12), e2024TC008280. https://doi.org/10.1029/2024TC008280

Ma, A., Hu, X., Kapp, P., Han, Z., Lai, W., & BouDagher-Fadel, M. (2018). The disappearance of a Late Jurassic remnant sea in the southern Qiangtang Block (Shamuluo Formation, Najiangco area): Implications for the tectonic uplift of central Tibet. *Palaeogeography, Palaeoclimatology, Palaeoecology*, *506*, 30–47. https://doi.org/10.1016/j.palaeo.2018.06.005

Ma, A., Hu, X., Li, X., Pullen, A., Garzanti, E., & Suzuki, N. (2024). Timing of rifting of the Dongkaco microcontinent (Central Tibet) and implications for Neo-Tethyan evolution. *Palaeogeography, Palaeoclimatology, Palaeoecology*, *638*, 112054. https://doi.org/10.1016/j.palaeo.2024.112054

Ma, A., Hu, X.-M., Garzanti, E., Han, Z., & Lai, W. (2017). Sedimentary and tectonic evolution of the southern Qiangtang basin: Implications for the Lhasa-Qiangtang collision timing. *Journal of Geophysical Research: Solid Earth*, *122*(7), 4790–4813. https://doi.org/10.1002/2017JB014211

Ma, A., Hu, X.-M., Kapp, P., BouDagher-Fadel, M., & Lai, W. (2020). Pre-Oxfordian (>163 Ma) ophiolite obduction in Central Tibet. *Geophysical Research Letters*, *47*(10), e2019GL086650. https://doi.org/10.1029/2019GL086650

Ma, A., Hu, X.-M., Kapp, P., Lai, W., Han, Z., & Xue, W.-W. (2020). Mesozoic subduction accretion history in central Tibet constrained from provenance analysis of the Mugagangri Subduction Complex in the Bangong-Nujiang suture zone. *Tectonics*, *39*(9), e2020TC006144. https://doi.org/10.1029/2020TC006144

Ma, L., Wang, B.-D., Jiang, Z.-Q., Wang, Q., Li, Z.-X., Wyman, D. A., et al. (2014). Petrogenesis of the Early Eocene adakitic rocks in the Napuri area, southern Lhasa: Partial melting of thickened lower crust during slab break-off and implications for crustal thickening in southern Tibet. *Lithos*, *196*, 321–338. https://doi.org/10.1016/j.lithos.2014.02.011

Malkowski, M. A., Johnstone, S. A., Sharman, G. R., White, C. J., Scheirer, D. S., & Barth, G. A. (2022). Continental shelves as detrital mixers: U–Pb and Lu–Hf detrital zircon provenance of the Pleistocene–Holocene Bering Sea and its margins. *The Depositional Record*, *8*(3), 1008–1030. https://doi.org/10.1002/dep2.203

Malkowski, M. A., Sharman, G. R., Johnstone, S. A., Grove, M. J., Kimbrough, D. L., & Graham, S. A. (2019). Dilution and propagation of provenance trends in sand and mud: Geochemistry and detrital zircon geochronology of modern sediment from central California (USA). *American Journal of Science*, *319*(10), 846–902. https://doi.org/10.2475/10.2019.02

Malusà, M. G., Resentini, A., & Garzanti, E. (2016). Hydraulic sorting and mineral fertility bias in detrital geochronology. *Gondwana Research*, *31*, 1–19. https://doi.org/10.1016/j.gr.2015.09.002

Miall, A. D. (1977). A review of the braided-river depositional environment. *Earth-Science Reviews*, *13*(1), 1–62. https://doi.org/10.1016/0012-8252(77)90055-1

Molnar, P., England, P., & Martinod, J. (1993). Mantle dynamics, uplift of the Tibetan Plateau, and the Indian monsoon. *Reviews of Geophysics*, *31*(4), 357–396. https://doi.org/10.1029/93RG02030

Murphy, M. A., Yin, A., Harrison, T. M., Dürr, S. B., Chen, Z., Ryerson, F. J., et al. (1997). Did the Indo-Asian collision alone create the Tibetan plateau? *Geology*, *25*(8), 719–722. https://doi.org/10.1130/0091-7613(1998)026<0958:DTIACA>2.3.CO;2

Mutti, E. (1985). Turbidite systems and their relations to depositional sequences. *Provenance of arenites* (pp. 65–93). https://doi.org/10.1007/978-94-017-2809-6_4

Paton, C., Hellstrom, J., Paul, B., Woodhead, J., & Hergt, J. (2011). Iolite: Freeware for the visualisation and processing of mass spectrometric data. *Journal of Analytical Atomic Spectrometry*, *26*(12), 2508–2518. https://doi.org/10.1039/c1ja10172b

Pickering, K. T., & Hiscott, R. N. (2015). *Deep marine systems: Processes, deposits, environments, tectonics and sedimentation*. American Geophysical Union, John Wiley & Sons.

Reading, H. G., & Richards, M. (1994). Turbidite systems in deep-water basin margins classified by grain size and feeder system. *AAPG Bulletin*, *78*(5), 792–822. https://doi.org/10.1306/A25FE3BF-171B-11D7-8645000102C1865D

Rohrmann, A., Kapp, P., Carrapa, B., Reiners, P. W., Guynn, J., Ding, L., & Heizler, M. (2012). Thermochronologic evidence for plateau formation in central Tibet by 45 Ma. *Geology*, *40*(2), 187–190. https://doi.org/10.1130/G32530.1

Rowley, D. B., & Currie, B. S. (2006). Palaeo-altimetry of the late Eocene to Miocene Lunpola basin, central Tibet. *Nature*, *439*(7077), 677–681. https://doi.org/10.1038/nature04506

Rubatto, D., & Gebauer, D. (2000). Use of cathodoluminescence for U-Pb zircon dating by ion microprobe: Some examples from the Western Alps. In *Cathodoluminescence in geosciences* (pp. 373–400). Springer. https://doi.org/10.1007/978-3-662-04086-7_15

Saylor, J. E., Jordan, J. C., Sundell, K. E., Wang, X., Wang, S., & Deng, T. (2018). Topographic growth of the Jishi Shan and its impact on basin and hydrology evolution, NE Tibetan Plateau. *Basin Research*, *30*(3), 544–563. https://doi.org/10.1111/bre.12264

Saylor, J. E., Sundell, K., & Sharman, G. (2019). Characterizing sediment sources by non-negative matrix factorization of detrital geochronological data. *Earth and Planetary Science Letters*, *512*, 46–58. https://doi.org/10.1016/j.epsl.2019.01.044

Saylor, J. E., & Sundell, K. E. (2016). Quantifying comparison of large detrital geochronology data sets. *Geosphere*, *12*(1), 203–220. https://doi.org/10.1130/GES01237.1

Sharman, G. R., & Johnstone, S. A. (2017). Sediment unmixing using detrital geochronology. *Earth and Planetary Science Letters*, *477*, 183–194. https://doi.org/10.1016/j.epsl.2017.07.044

Sharman, G. R., Sharman, J. P., & Sylvester, Z. (2018). detritalPy: A Python-based toolset for visualizing and analysing detrital geothermochronologic data. *The Depositional Record*, *4*(2), 202–215. https://doi.org/10.1002/dep2.45

Sláma, J., Košler, J., Condon, D. J., Crowley, J. L., Gerdes, A., Hanchar, J. M., et al. (2008). Plešovice zircon—A new natural reference material for U–Pb and Hf isotopic microanalysis. *Chemical Geology*, *249*(1–2), 1–35. https://doi.org/10.1016/j.chemgeo.2007.11.005

Song, B., Zhang, K., Wei, Y., Jiang, G., Yang, T., Algeo, T. J., et al. (2023). Paleogene sediment provenance in the Gaize Basin: Implications for early Cenozoic paleogeography of central Tibet. *Palaeogeography, Palaeoclimatology, Palaeoecology*, *632*, 111860. https://doi.org/10.1016/j.palaeo.2023.111860

Spencer, C. J., Kirkland, C. L., & Roberts, N. M. (2018). Implications of erosion and bedrock composition on zircon fertility: Examples from South America and Western Australia. *Terra Nova*, *30*(4), 289–295. https://doi.org/10.1111/ter.12338

Spicer, R. A., Farnsworth, A., Su, T., Ding, L., Witkowski, C. R., Li, S.-F., et al. (2025). The progressive co-evolutionary development of the Pan-Tibetan highlands, the Asian Monsoon system and Asian Biodiversity. *Geological Society, London, Special Publications*, *549*(1), SP549-2023-2180. https://doi.org/10.1144/SP549-2023-18

Stacey, J. T., & Kramers, J. (1975). Approximation of terrestrial lead isotope evolution by a two-stage model. *Earth and Planetary Science Letters*, *26*(2), 207–221. https://doi.org/10.1016/0012-821X(75)90088-6

Su, T., Farnsworth, A., Spicer, R. A., Huang, J., Wu, F.-X., Liu, J., et al. (2019). No high Tibetan plateau until the Neogene. *Science Advances*, *5*(3), eaav2189. https://doi.org/10.1126/sciadv.aav2189

Su, T., Spicer, R. A., Wu, F.-X., Farnsworth, A., Huang, J., Del Rio, C., et al. (2020). A Middle Eocene lowland humid subtropical "Shangri-La" ecosystem in central Tibet. *Proceedings of the National Academy of Sciences*, *117*(52), 32989–32995. https://doi.org/10.1073/pnas.2012647117

Sun, G., Hu, X., Xu, Y., & BouDagher-Fadel, M. K. (2019). Discovery of Middle Jurassic trench deposits in the Bangong-Nujiang suture zone: Implications for the timing of Lhasa-Qiangtang initial collision. *Tectonophysics*, *750*, 344–358. https://doi.org/10.1016/j.tecto.2018.12.001

Sun, S.-S., & McDonough, W. F. (1989). Chemical and isotopic systematics of oceanic basalts: Implications for mantle composition and processes. *Geological Society, London, Special Publications*, *42*(1), 313–345. https://doi.org/10.1144/GSL.SP.1989.042.01.1

Surlyk, F. (1978). Submarine fan sedimentation along fault scarps on tilted fault blocks (Jurassic-Cretaceous boundary, East Greenland). *Bulletin Grønlands Geologiske Undersøgelse*, *128*, 1–108. https://doi.org/10.34194/bullggu.v128.6670

Tang, Y., Zhai, Q.-G., Chung, S.-L., Hu, P.-Y., Wang, J., Xiao, X.-C., et al. (2020). First mid-ocean ridge-type ophiolite from the Meso-Tethys suture zone in the north-central Tibetan plateau. *Geological Society of America Bulletin*, *132*(9–10), 2202–2220. https://doi.org/10.1130/B35500.1

Wang, C., Zhao, X., Liu, Z., Lippert, P. C., Graham, S. A., Coe, R. S., et al. (2008). Constraints on the early uplift history of the Tibetan Plateau. *Proceedings of the National Academy of Sciences*, *105*(13), 4987–4992. https://doi.org/10.1073/pnas.0703595105

Wang, L., Wang, C., Li, Y., Zhu, L., & Wei, Y. (2011). Organic geochemistry of potential source rocks in the Tertiary Dingqinghu Formation, Nima basin, central Tibet. *Journal of Petroleum Geology*, *34*(1), 67–85. https://doi.org/10.1111/j.1747-5457.2011.00494.x

Wang, Q., Zhu, D. C., Cawood, P. A., Chung, S. L., & Zhao, Z. D. (2021). Resolving the paleogeographic puzzle of the Lhasa Terrane in southern Tibet. *Geophysical Research Letters*, *48*(15), e2021GL094236. https://doi.org/10.1029/2021GL094236

Wang, Z., Wang, Y.-S., & Xie, Y.-H. (2005). The Tarenben oceanic-island basalts in the middle part of the Bangong-Nujiang suture zone, Xizang and their geological implications. *Sedimentary Geology and Tethyan Geology*, *25*(1/2), 155.

Watson, E. B., & Harrison, T. (2005). Zircon thermometer reveals minimum melting conditions on earliest Earth. *Science*, *308*(5723), 841–844. https://doi.org/10.1126/science.111087

Wei, Y., Zhang, K., Garzione, C. N., Xu, Y., Song, B., & Ji, J. (2016). Low palaeoelevation of the northern Lhasa terrane during late Eocene: Fossil foraminifera and stable isotope evidence from the Gerze Basin. *Scientific Reports*, *6*(1), 27508. https://doi.org/10.1038/srep27508

Wu, F., Miao, D., Chang, M.-M., Shi, G., & Wang, N. (2017). Fossil climbing perch and associated plant megafossils indicate a warm and wet central Tibet during the late Oligocene. *Scientific Reports*, *7*(1), 878. https://doi.org/10.1038/s41598-017-00928-9

Xia, D. X., & Liu, S. K. (1997). *Lithostratigraphy of Xizang (Tibet) Autonomous Region* (in Chinese with English abstract). China University of Geosciences Press.

Xiong, Z., Liu, X., Ding, L., Farnsworth, A., Spicer, R. A., Xu, Q., et al. (2022). The rise and demise of the Paleogene Central Tibetan Valley. *Science Advances*, *8*(6), eabj0944. https://doi.org/10.1126/sciadv.abj0944

Xu, Y., Hu, X., Garzanti, E., BouDagher-Fadel, M., Sun, G., Lai, W., & Zhang, S. (2022). Mid-Cretaceous thick carbonate accumulation in Northern Lhasa (Tibet): Eustatic vs. tectonic control? *Bulletin*, *134*(1–2), 389–404. https://doi.org/10.1130/B35930.1

Yan, L.-L., & Zhang, K.-J. (2020). Infant intra-oceanic arc magmatism due to initial subduction induced by oceanic plateau accretion: A case study of the Bangong Meso-Tethys, central Tibet, western China. *Gondwana Research*, *79*, 110–124. https://doi.org/10.1016/j.gr.2019.08.008

Yang, Z.-Y., Wang, Q., Hao, L.-L., Wyman, D. A., Ma, L., Wang, J., et al. (2021). Subduction erosion and crustal material recycling indicated by adakites in central Tibet. *Geology*, *49*(6), 708–712. https://doi.org/10.1130/G48486.1

Yousefi, F., & Lentz, D. R. (2024). Formation of high-silica adakites and their relationship with slab break-off: Implications for generating fertile Cu-Au-Mo porphyry systems. *Geoscience Frontiers*, *15*(6), 101927. https://doi.org/10.1016/j.gsf.2024.101927

Zhang, K.-J., Xia, B., Zhang, Y. X., Liu, W. L., Zeng, L., Li, J. F., & Xu, L. F. (2014). Central Tibetan Meso-Tethyan oceanic plateau. *Lithos*, *210*, 278–288. https://doi.org/10.1016/j.lithos.2014.09.004

Zhang, Q.-H., Ding, L., Cai, F.-L., Xu, X.-X., Zhang, L.-Y., Xu, Q., & Willems, H. (2011). Early Cretaceous Gangdese retroarc foreland basin evolution in the Selin Co basin, central Tibet: Evidence from sedimentology and detrital zircon geochronology. *Geological Society, London, Special Publications*, *353*(1), 27–44. https://doi.org/10.1144/sp353.3

Zhang, W.-Q., Liu, C.-Z., Liu, T., Zhang, C., & Zhang, Z.-Y. (2021). Subduction initiation triggered by accretion of a Jurassic oceanic plateau along the Bangong–Nujiang Suture in central Tibet. *Terra Nova*, *33*(2), 150–158. https://doi.org/10.1111/ter.12500

Zhu, D.-C., Li, S.-M., Cawood, P. A., Wang, Q., Zhao, Z.-D., Liu, S.-A., & Wang, L.-Q. (2016). Assembly of the Lhasa and Qiangtang terranes in central Tibet by divergent double subduction. *Lithos*, *245*(1), 7–17. https://doi.org/10.1139/e17-005

Zhu, Z., Zhai, Q., Hu, P., Tang, Y., Wang, H., Wang, W., & Wu, H. (2022). Resolving the timing of Lhasa-Qiangtang block collision: Evidence from the Lower Cretaceous Duoni Formation in the Baingoin foreland basin. *Palaeogeography, Palaeoclimatology, Palaeoecology*, *595*, 110956. https://doi.org/10.1016/j.palaeo.2022.110956

Zhu, Z., Zhai, Q.-G., Hu, P.-Y., Chung, S.-L., Tang, Y., Wang, H.-T., et al. (2019). Closure of the Bangong–Nujiang Tethyan Ocean in the central Tibet: Results from the provenance of the Duoni Formation. *Journal of Sedimentary Research*, *89*(10), 1039–1054. https://doi.org/10.2110/jsr.2019.55